Ocean Engineering 363 (2026) 126741

Contents lists available at ScienceDirect

Ocean Engineering

journal homepage: www.elsevier.com/locate/oceaneng

ELSEVIER

Research paper

Irregular wave-based analysis of prediction horizon length in model predictive control for a point absorber wave energy converter

Md Shahidullah Kaiser, Takahito Iida *, Ryo Yoshimura

Department of Naval Architecture and Ocean Engineering, The University of Osaka, Suita, Osaka 5650871, Japan

ARTICLE INFO

Keywords:
Point absorber wave energy converter
Energy absorption efficiency
Model predictive control
Superposition principle
Prediction horizon length

ABSTRACT

The prediction horizon length is a crucial parameter in model predictive control (MPC) that determines how far in advance the future wave exciting force must be predicted for real-time control. This paper presents an optimal solution for the prediction horizon length in MPC for a point absorber wave energy converter (PA-WEC) operating under irregular wave conditions. To maximize absorption power and energy absorption efficiency, the dimensions of the floating body of PA-WEC are tuned according to the sea state. The linear superposition principle is investigated within the MPC formulation to assess its applicability and to determine whether the absorbed power under irregular waves can be represented as a superposition of the corresponding regular wave components. The resulting absorbed power is compared with that obtained using a constant damping control method as a reference. Finally, an empirical solution for identifying the optimal prediction horizon length in MPC for irregular waves is proposed based on the wave spectrum.

1. Introduction

In recent years, global society has paid attention to renewable energy sources owing to the depletion of fossil fuel reserves, leading to notable increases in the prices of natural gas and oil (Zhang et al., 2021). Additionally, it is necessary to address the requirement of mitigating greenhouse gas emissions (Khedkar and Bhalla, 2022). Worldwide energy consumption was approximately 170,000 TWh in 2023 (MSCI, 2023), and is estimated to increase by up to 56% by 2040 (Alkhatib et al., 2020). This growing energy demand has accumulated interest in ocean renewable energy as a viable source, offering enormous energy while emitting net-zero carbon. The entire ocean has the potential to produce around 8000-80,000 TWh of wave energy annually (Zullah and Lee, 2013). A prominent aspect of ocean wave energy is its higher energy density and greater predictability compared with solar and wind energy (Hernández-Robles et al., 2021), while also having minimal environmental impact. Numerous concepts of wave energy converters (WECs) have been developed to harness ocean wave energy. The point absorber wave energy converter (PA-WEC) is the most promising WEC concept proposed to date (Falnes, 2002) and comprises more than 81% of WECs (Reabroy et al., 2019). The PA-WEC is widely appreciated for its simplicity in design and operational principles, as well as its compact size and cost-effectiveness (Gao and Xiao, 2021). For commercial purposes, the concept of a wave farm can be implemented, which is the deployment of PA-WECs in arrays of multiple units (Han et al., 2023). Despite the enormous potential of PA-WEC, commercial deployment has yet to succeed in comparison to other renewable energy sources. The primary challenge of commercializing PA-WECs is the increased levelized cost of energy (LCoE) (Tan et al., 2022). To reduce LCoE, it is crucial to enhance the energy absorption efficiency of the PA-WEC. However, the irregular wave exciting forces of incoming ocean waves complicate the task of the controller in optimizing PA-WEC's performance. One of the most effective methods for facilitating optimum interaction between the PA-WEC and incident waves is the implementation of a real-time advanced control strategy. This approach increases energy absorption efficiency and reduces LCoE (Ling et al., 2020).

Numerous control strategies have been developed over the past few decades to optimize control force in real-time and improve absorption efficiency, including reactive control (Evans, 1981; Pizer, 1993; Naito and Nakamura, 1986), latching control (Babarit and Clément, 2006), declutching control (Eidsmoen, 1998; Babarit et al., 2009), and complex conjugate control (Fusco and Ringwood, 2013). Additionally, control strategies for WECs have been integrated with artificial intelligence (AI) techniques, including deep reinforcement learning (DRL) (Zou et al., 2022), long short-term memory (LSTM) (Yin and Jiang, 2023), thereby enhancing control performance and enabling the development of several novel, adaptive control methods (Liang et al., 2024). Among all the control schemes investigated in WECs, model predictive control (MPC) is the most well-developed strategy (Todalshaug et al.,

* Corresponding author.
E-mail address: iida@naoe.eng.osaka-u.ac.jp (T. Iida).

https://doi.org/10.1016/j.oceaneng.2026.126741
Received 29 January 2026; Received in revised form 12 June 2026; Accepted 25 June 2026
Available online 2 July 2026

2011; Li and Belmont, 2014), leading to significant improvements in power generation (Coe et al., 2017), approaching the theoretical optimum value (Nguyen et al., 2016), and can even be integrated with an AI model such as LSTM (Zhang et al., 2024). An advantageous aspect of MPC is its ability to efficiently manage constraints, as demonstrated in numerous cases involving displacement (Brekken, 2011; Hals et al., 2010a; Jama et al., 2014), velocities (O'Sullivan and Lightbody, 2017), and control forces (Hals et al., 2010a; Montoya Andrade et al., 2014), while maximizing power output. This control method employs future wave exciting forces to determine a sequence of power take-off (PTO) control forces over a specified prediction horizon length at each sampling interval, while accounting for constraints (Umeda et al., 2024) and optimizing the future control forces for the PA-WEC. For real-time control in PA-WECs, accurately predicting future wave exciting forces is essential. However, due to the presence of non-causality, it is challenging to accurately predict these future wave exciting forces in advance. This high dependence on future wave exciting forces complicates the implementation of control strategies, especially MPC, in PA-WECs (Ling et al., 2020; Nguyen and Tona, 2018). To overcome this difficulty, most studies associated with MPC in PA-WECs have used precomputed predictions of wave exciting forces for real-time implementation. The incident wave elevation and wave exciting force can be predicted using measurements and past wave information data. The prediction of water waves has recently been developed using the impulse response function (Iida and Minoura, 2022), and, based on this approach, the wave exciting forces can be predicted accurately (Yoshimura et al., 2025). As a result, the primary challenge with MPC in PA-WEC is determining how far in advance we need to predict the future wave exciting force, which introduces a crucial parameter: the prediction horizon length.

The prediction horizon length in MPC denotes the time length (Afram and Janabi-Sharifi, 2014), and in this study, it indicates the time over which the controller optimizes the PTO control force based on the future wave exciting force at each sampling interval while considering constraints. Therefore, both the prediction horizon length and the sampling interval, collectively referred to as the time horizon, determine how far in advance the future wave exciting force must be predicted. The time horizon can be adjusted either by employing (i) a large sampling interval with a short prediction horizon length, or (ii) a small sampling interval with a long prediction horizon length (Kaiser et al., 2025). A large sampling interval with a short prediction horizon length can reduce the computation time required to solve the optimization process (Sergiienko et al., 2021). However, this procedure reduces the accuracy of the motion calculation (Yang et al., 2021; Bøhn et al., 2021) and cannot encompass sufficient information about the future wave exciting force (Wu et al., 2022). As a result, a small sampling interval with a long prediction horizon length is recommended to determine the time horizon. Nonetheless, if the sampling interval is excessively small (for instance, less than 100 ms) (Li et al., 2011), computational costs will increase (Osinenko and Dobriborsci, 2021), thereby complicating real-time implementation. A moderate value for the small sampling interval has recently been introduced, achieving higher energy absorption efficiency (Kaiser et al., 2025). The remaining concern is the appropriate length of the prediction horizon length. A significantly long prediction horizon does not consistently yield high efficiency; rather, it can result in high computational time (Wu et al., 2022). Additionally, in these circumstances, higher PTO control forces are required; as a result, the controller's behavior becomes more aggressive (Sergiienko et al., 2021). Moreover, the prediction accuracy of the wave exciting force decreases with increasing prediction horizon length (Hillis et al., 2020). For this reason, the prediction horizon length in MPC is sensitive to both real-time optimization performance (Genest and Ringwood, 2016) and overall system performance (Hillis et al., 2020). Once the optimal prediction horizon length is identified, it is straightforward to predict the future wave exciting force within this time frame, allowing MPC to optimize the PTO control forces to maximize energy absorption efficiency. Therefore, it is necessary to investigate the prediction horizon length in MPC in order to determine the optimal solution.

Several strategies have been recommended for determining the prediction horizon length to ensure optimal MPC performance; one approach is based on experimentation (Bertsekas, 1995). Additionally, other proposals include selecting the prediction horizon length by aligning it with the incident wave period (Genest and Ringwood, 2016) or the natural period of the system (Hals et al., 2010b). The optimal solution of prediction horizon length in MPC for PA-WEC has recently been established under the regular wave case (Kaiser et al., 2025). If a linear state-space model is employed to describe any PA-WEC, this MPC formulation can be applied. In addition, by comprising the sequence of future wave exciting forces, this empirical optimal solution for the prediction horizon length effectively indicates how far in advance the future wave exciting force must be predicted, thereby maximizing absorbed power and energy absorption efficiency by a PA-WEC. Although the optimal solution for the prediction horizon length in regular waves is important, in practical operations, PA-WEC must operate mostly in irregular sea elevations resulting from the superposition of regular waves. However, the corresponding optimal prediction horizon length under irregular waves has not yet been determined. In such a case, the proposed optimal solution for the prediction horizon length in MPC for the regular wave case (Kaiser et al., 2025) may not be directly applicable for the irregular wave applications. Therefore, it is essential to determine the optimal prediction horizon length for irregular wave sea state conditions.

Motivated by the considerations outlined above, this study proposes an optimal solution for the prediction horizon length in MPC for PA-WEC under irregular wave conditions, which constitutes the primary novelty of this study. This analysis will enable the assessment of how far in advance the future wave exciting force needs to be predicted for real-time control in order to maximize energy absorption efficiency under sea state conditions. Based on the sea state information, the wave spectrum of irregular waves is obtained, and its accuracy is validated through frequency and time domain analyses. The dimensions of the floating body of the PA-WEC are adjusted in accordance with the sea state to achieve the maximum resonance condition. To validate the absorbed power under irregular waves, the linear superposition principle has been employed, whereby the absorbed power under irregular waves is equal to the sum of the absorbed power associated with the regular wave components that constitute the irregular wave (Murai and Iikura, 2020). Although this principle has previously been applied for the damping control method (Murai and Iikura, 2020), its applicability to MPC has not yet been evaluated. Therefore, as another novelty in this study, the linear superposition principle is investigated in MPC to assess its applicability for validating absorbed power. Furthermore, the absorbed power and energy absorption efficiency of MPC are compared with those obtained using a constant damping control force as a reference. Finally, the optimal solution for the prediction horizon length in MPC is proposed for the irregular wave case.

2. Theory

2.1. Equation of motion

The schematic representation of a two-dimensional PA-WEC, along with the forces acting on it, is illustrated in Fig. 1 using horizontal and vertical planes. The floating body is considered symmetric, and its shape is described by the Lewis form (Kashiwagi et al., 2006) with a sectional area ratio $\sigma = 0.9$. The origin O is located on the undisturbed still water free-surface, from which the waves propagate unidirectionally in the positive x direction. The fluid is assumed to be incompressible, inviscid, and irrotational, with a linear model used for simplicity and low computational cost in wave-body interaction simulations (Holthuijsen, 2007). Since axisymmetric PA-WEC primarily captures energy through heave motion (Khedkar and Bhalla, 2022), this

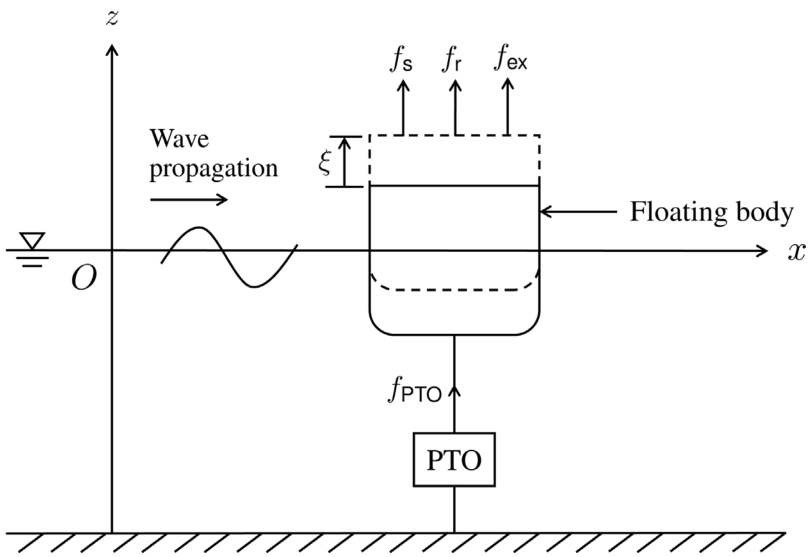

Fig. 1. Schematic representation of a two-dimensional PA-WEC with one DOF heave motion, along with the forces acting on it. Waves propagate unidirectionally in the positive x direction. The solid and dashed outlines of the floating body denote its position at rest, and its vertical displacement ξ relative to the equilibrium position, respectively. The control force is exerted on the floating body by the PTO system.

study considers the PA-WEC to oscillate with one degree of freedom (DOF) in heave direction with its vertical displacement ξ measured with respect to the hydrostatic equilibrium position. The motion amplitude of the body is minimal compared to the wave height; therefore, using linear potential theory (Newman, 1977), the total force exerted on the body can be represented by the sum of the radiation force f_r, hydrostatic restoring force f_s, and wave exciting force f_ex. The control force f_PTO is exerted by the PA-WEC controller integrated with a PTO system, which retards the wave-induced body motion to extract energy. In this problem formulation, the PTO mechanism is assumed to be ideal. Based on Newton's second law of motion, the linearized motion equation in the time domain for the PA-WEC can be expressed as

$$m\ddot{\xi}(t) = f_\mathrm{s}(t) + f_\mathrm{r}(t) + f_\mathrm{ex}(t) + f_\mathrm{PTO}(t), \tag{1}$$

where t denotes time, and m and $\ddot{\xi}$ represent the mass and acceleration of the body, respectively. The hydrostatic restoring force f_s resulting from buoyancy is determined by

$$f_\mathrm{s}(t) = -C_\mathrm{s}\xi(t), \tag{2}$$

Here, hydrostatic stiffness is defined as $C_\mathrm{s} = \rho g A_W$, in which ρ, g, and A_W represent fluid density, gravitational acceleration, and waterline area of the body, respectively.

The radiation force f_r is modeled as the sum of a convolution integral of the radiation impulse response function h_rad with the floating body's velocity $\dot{\xi}$ and an added mass component that is proportional to the acceleration of the floating body $\ddot{\xi}$. The radiation force f_r is defined as

$$f_\mathrm{r}(t) = -A(\infty)\ddot{\xi}(t) - \int_{-\infty}^{t} \dot{\xi}(\tau)h_\mathrm{rad}(t-\tau)d\tau, \tag{3}$$

In this case, $A(\infty)$ is the added mass term when frequency ω tends to infinity. The radiation impulse response function h_rad can be calculated by integrating the hydrodynamic coefficients, $A(\omega)$ and $B(\omega)$, which represent the added mass and the damping coefficient, respectively, within the frequency domain, as mentioned in Falnes (2002)

$$h_\mathrm{rad}(t) = -\frac{2}{\pi}\int_0^\infty \omega\{A(\omega) - A(\infty)\}\sin(\omega t)d\omega = \frac{2}{\pi}\int_0^\infty B(\omega)\cos(\omega t)d\omega, \tag{4}$$

Based on the deep-water assumption, an in-house 2D boundary element method (BEM) code is employed to compute the hydrodynamic coefficients for the radiation force and the wave exciting force in the frequency domain, as detailed in Kaiser et al. (2025).

The equation of motion of the PA-WEC outlined in Eq. (1) must be represented as a state-space model to facilitate the implementation of the MPC method discussed in the following section. Eq. (4) provides only the sampled data of the radiation impulse response function h_rad, rather than an analytical expression. Therefore, Prony's method is applied to the sampled data of the radiation impulse response function h_rad obtained by 2D-BEM to approximate the function h_rad as a sum of exponential functions (Duclos et al., 2000). Consequently, the convolution integral term in Eq. (3) can be expressed as

$$I(t) = \sum_{i=1}^{n}\left[\int_0^t \dot{\xi}(\tau)\alpha_i e^{\beta_i(t-\tau)}d\tau\right] = \sum_{i=1}^{n} I_i(t), \tag{5}$$

where $\{\alpha_i, \beta_i\}_{i=1}^n$ are the complex coefficients of Prony's method. In this study, an approximation order of $n = 10$ is employed, which is adequate for convergence, as illustrated in Fig. A.10. The final expression of the motion equation in the time domain is referred to as Cummins' equation (Cummins, 1962), which is expressed as follows:

$$\ddot{\xi}(t) = \frac{1}{M}\left[-C_\mathrm{s}\xi(t) - \sum_{i=1}^{n} I_i^R(t) + f_\mathrm{ex}(t) + f_\mathrm{PTO}(t)\right]. \tag{6}$$

Here, the total mass of the system is denoted by $M = m + A(\infty)$, and $I_i^R(t)$ represents the real part of the solution $I_i(t)$ of the ordinary differential equation.

2.2. Control strategy

Two control strategies are employed in this study for comparison: constant damping control and MPC. The following subsections present an overview of these two control methods.

2.2.1. Constant damping control method

Prior to applying the MPC method, the PA–WEC is analyzed using a linear damping control method, which serves as a reference for comparing the MPC-computed responses. Here, a damping force f_v is referred to as the control force, exerted by an external damper. By substituting the damping control force f_v instead of the control force f_PTO by the PTO unit, the time domain motion equation Eq. (6) can be modified

$$\ddot{\xi}(t) = \frac{1}{M}\left[-C_\mathrm{s}\xi(t) - \sum_{i=1}^{n} I_i^R(t) + f_\mathrm{ex}(t) + f_v(t)\right], \tag{7}$$

For irregular wave analysis, the damping force is defined as

$$f_v = -v\dot{\xi}(t), \tag{8}$$

where $v = B(\omega_i)$ is the constant damping coefficient corresponding to a representative wave frequency ω_i as stated in Korde and Ertekin (2015). Accordingly, this approach will be designated as the constant damping control method throughout this study. The time domain motion equation Eq. (7) of the PA-WEC is transformed to the frequency domain, resulting in

$$\Xi(\omega) = \frac{F_{\text{ex}}(\omega)}{[-\omega^2\{m + A(\omega)\} + i\omega\{B(\omega) + v\} + C_s]}. \tag{9}$$

Here, F_{ex} and Ξ are the complex amplitudes of the wave exciting force and the displacement of the floating body in the frequency domain, respectively.

2.2.2. Model predictive control

i. **State-space representation**

First, the convolution integral term in Eq. (3) is replaced by the radiation state-space model as

$$\begin{aligned} \dot{\boldsymbol{x}}_{\text{rad}}(t) &= \boldsymbol{A}_{\text{rad}}\boldsymbol{x}_{\text{rad}}(t) + \boldsymbol{B}_{\text{rad}}\dot{\xi}(t), \\ \int_{-\infty}^{t} \dot{\xi}(\tau)h_{\text{rad}}(t-\tau)d\tau &\approx \boldsymbol{C}_{\text{rad}}\boldsymbol{x}_{\text{rad}}(t), \end{aligned} \tag{10}$$

where $\boldsymbol{x}_{\text{rad}} \in \mathbb{R}^{n\times 1}$ is the state vector and $\boldsymbol{A}_{\text{rad}}$, $\boldsymbol{B}_{\text{rad}}$, and $\boldsymbol{C}_{\text{rad}}$ are the state-space matrices of the radiation component, defined as follows:

$$\boldsymbol{A}_{\text{rad}} = \begin{bmatrix} -q_1 & -q_2 & \cdots & -q_{n-1} & -q_n \\ 1 & 0 & \cdots & 0 & 0 \\ 0 & 1 & \cdots & 0 & 0 \\ \vdots & \vdots & \ddots & \vdots & \vdots \\ 0 & 0 & \cdots & 1 & 0 \end{bmatrix} \in \mathbb{R}^{n\times n},$$

$$\boldsymbol{B}_{\text{rad}} = \begin{bmatrix} 1 & 0 & 0 & \cdots & 0 \end{bmatrix}^{\mathrm{T}} \in \mathbb{R}^{n\times 1},$$

$$\boldsymbol{C}_{\text{rad}} = \begin{bmatrix} p_1 & p_2 & \cdots & p_{n-1} & p_n \end{bmatrix} \in \mathbb{R}^{1\times n}.$$

Here, $\{p_i, q_i\}_{i=0}^{n}$ are polynomial coefficients with $q_0 = 1$ of the radiation transfer function $H_{\text{rad}}(s)$, which is the Laplace transform of the radiation impulse response function h_{rad}. Using the motion equation Eq. (6) and the radiation state-space model Eq. (10), the state-space continuous time model for the whole PA-WEC can be written as

$$\begin{aligned} \dot{\boldsymbol{x}}_c(t) &= \boldsymbol{A}_c\boldsymbol{x}_c(t) + \boldsymbol{B}_c(f_{\text{ex},c}(t) + f_{\text{PTO},c}(t)), \\ \boldsymbol{y}_c(t) &= \boldsymbol{C}_c\boldsymbol{x}_c(t), \end{aligned} \tag{11}$$

where the quantities of continuous-time are denoted by subscript c, and the corresponding vectors and matrices of the whole PA-WEC are given by

$$\boldsymbol{x}_c = \begin{bmatrix} \xi \\ \dot{\xi} \\ \boldsymbol{x}_{\text{rad}} \end{bmatrix} \in \mathbb{R}^{(n+2)\times 1}, \quad \boldsymbol{y}_c = \begin{bmatrix} \xi \\ \dot{\xi} \end{bmatrix} \in \mathbb{R}^{2\times 1},$$

$$\boldsymbol{A}_c = \begin{bmatrix} 0 & 1 & \boldsymbol{0} \\ \frac{-C_s}{M} & 0 & \frac{-1}{M}\boldsymbol{C}_{\text{rad}} \\ \boldsymbol{0} & \boldsymbol{B}_{\text{rad}} & \boldsymbol{A}_{\text{rad}} \end{bmatrix} \in \mathbb{R}^{(n+2)\times(n+2)},$$

$$\boldsymbol{B}_c = \begin{bmatrix} 0 \\ \frac{1}{M} \\ \boldsymbol{0} \end{bmatrix} \in \mathbb{R}^{(n+2)\times 1},$$

$$\boldsymbol{C}_c = \begin{bmatrix} 1 & 0 & \boldsymbol{0} \\ 0 & 1 & \boldsymbol{0} \end{bmatrix} \in \mathbb{R}^{2\times(n+2)}.$$

The notation $\boldsymbol{0}$ represents a zero matrix of specified dimensions.

ii. **Discretization**

This study employs the first-order hold method described in Cretel et al. (2011) to discretize the continuous-time model Eq. (11). If the current state $\boldsymbol{x}_\delta(k)$ advances to the next state $\boldsymbol{x}_\delta(k+1)$ with a sampling interval $T_s > 0$ and a discrete time index is k, where $\forall k \in \mathbb{N}$, the discretized form of continuous-time model Eq. (11) can be written as

$$\begin{aligned} \boldsymbol{x}_\delta(k+1) &= \boldsymbol{\varphi}(T_s)\boldsymbol{x}_\delta(k) + \boldsymbol{\Gamma}(f_{\text{ex},\delta}(k) + f_{\text{PTO},\delta}(k)) \\ &\quad + \boldsymbol{\Psi}(\Delta f_{\text{ex}}(k+1) + \Delta f_{\text{PTO}}(k+1)), \\ \boldsymbol{y}_\delta(k) &= \boldsymbol{C}_c\boldsymbol{x}_\delta(k), \end{aligned} \tag{12}$$

In this study, the discretized quantities are indicated by the subscript δ. Accordingly, Δf_{ex} and Δf_{PTO} represent the increments of the discretized wave exciting forces and control forces, respectively. The relations used in Eq. (12) are outlined below

$$\begin{aligned} \boldsymbol{\varphi}(t) &= \exp(\boldsymbol{A}_c t) \in \mathbb{R}^{(n+2)\times(n+2)}, \\ \boldsymbol{\Gamma} &= \boldsymbol{A}_c^{-1}(\boldsymbol{\varphi}(T_s) - \mathbf{I})\boldsymbol{B}_c \in \mathbb{R}^{(n+2)\times 1}, \\ \boldsymbol{\Psi} &= \frac{1}{T_s}\boldsymbol{A}_c^{-1}\left(\boldsymbol{\Gamma} - T_s\boldsymbol{B}_c\right) \in \mathbb{R}^{(n+2)\times 1}, \\ f_{\text{ex},c}(t) &= f_{\text{ex},\delta}(k) + \left(\frac{t - kT_s}{T_s}\right)\Delta f_{\text{ex}}(k+1), \\ f_{\text{PTO},c}(t) &= f_{\text{PTO},\delta}(k) + \left(\frac{t - kT_s}{T_s}\right)\Delta f_{\text{PTO}}(k+1), \\ \Delta f_{\text{ex}}(k+1) &= f_{\text{ex},\delta}(k+1) - f_{\text{ex},\delta}(k), \\ \Delta f_{\text{PTO}}(k+1) &= f_{\text{PTO},\delta}(k+1) - f_{\text{PTO},\delta}(k). \end{aligned} \tag{13}$$

The corresponding vectors and matrices used in the discretized continuous-time model Eq. (12) are defined as follows:

$$\boldsymbol{x}_\delta = \begin{bmatrix} \boldsymbol{x}_c(kT_s) \\ f_{\text{ex},\delta} \\ f_{\text{PTO},\delta} \end{bmatrix} \in \mathbb{R}^{(n+4)\times 1}, \quad \boldsymbol{y}_\delta = \begin{bmatrix} \boldsymbol{y}_c(kT_s) \\ f_{\text{PTO},\delta} \end{bmatrix} \in \mathbb{R}^{3\times 1},$$

$$\boldsymbol{A}_\delta = \begin{bmatrix} \boldsymbol{\varphi}(T_s) & \boldsymbol{\Gamma} & \boldsymbol{\Gamma} \\ 0 & 1 & 0 \\ 0 & 0 & 1 \end{bmatrix} \in \mathbb{R}^{(n+4)\times(n+4)},$$

$$\boldsymbol{B}_\delta = \begin{bmatrix} \boldsymbol{\Psi} \\ 1 \\ 0 \end{bmatrix} \in \mathbb{R}^{(n+4)\times 1},$$

$$\boldsymbol{F}_\delta = \begin{bmatrix} \boldsymbol{\Psi} \\ 0 \\ 1 \end{bmatrix} \in \mathbb{R}^{(n+4)\times 1},$$

$$\boldsymbol{C}_\delta = \begin{bmatrix} 1 & 0 & 0 & \cdots & 0 & 0 & 0 \\ 0 & 1 & 0 & \cdots & 0 & 0 & 0 \\ 0 & 0 & 0 & \cdots & 0 & 1 & 0 \end{bmatrix} \in \mathbb{R}^{3\times(n+4)}. \tag{14}$$

iii. **MPC formulation**

The discretized model Eq. (12) propagates from $k+1$ up to the prediction horizon length N, resulting in the output prediction vector $\underline{\boldsymbol{Y}}$ is given by

$$\underline{\boldsymbol{Y}}(k) = \left[\boldsymbol{y}_\delta(k+i \mid k)\right]_{i=1}^{N} \in \mathbb{R}^{N\times 1} = \boldsymbol{\mathcal{T}}_x\boldsymbol{x}_\delta(k) + \boldsymbol{\mathcal{T}}_e\underline{\boldsymbol{\Delta f}}_{\text{ex}}(k) + \boldsymbol{\mathcal{T}}_p\underline{\boldsymbol{\Delta f}}_{\text{PTO}}(k), \tag{15}$$

where the increment prediction vectors of the wave exciting forces $\underline{\boldsymbol{\Delta f}}_{\text{ex}}$ and control forces $\underline{\boldsymbol{\Delta f}}_{\text{PTO}}$ are respectively defined as

$$\underline{\boldsymbol{\Delta f}}_{\text{ex}}(k) = \left[\Delta f_{\text{ex}}(k+i \mid k)\right]_{i=1}^{N} \in \mathbb{R}^{N\times 1}, \tag{16}$$

$$\underline{\boldsymbol{\Delta f}}_{\text{PTO}}(k) = \left[\Delta f_{\text{PTO}}(k+i \mid k)\right]_{i=1}^{N} \in \mathbb{R}^{N\times 1}, \tag{17}$$

The matrices used in Eq. (15) are defined as follows

$$\boldsymbol{\mathcal{T}}_x = \begin{bmatrix} \boldsymbol{C}_\delta\boldsymbol{A}_\delta \\ \boldsymbol{C}_\delta\boldsymbol{A}_\delta^2 \\ \vdots \\ \boldsymbol{C}_\delta\boldsymbol{A}_\delta^N \end{bmatrix} \in \mathbb{R}^{3N\times(n+4)},$$

$$\mathcal{T}_e = \begin{bmatrix} C_\delta B_\delta & 0 & 0 & \cdots & 0 \\ C_\delta A_\delta B_\delta & C_\delta B_\delta & 0 & \cdots & 0 \\ C_\delta A_\delta^2 B_\delta & C_\delta A_\delta B_\delta & C_\delta B_\delta & \cdots & 0 \\ \vdots & \vdots & \vdots & \ddots & \vdots \\ C_\delta A_\delta^{N-1} B_\delta & C_\delta A_\delta^{N-2} B_\delta & C_\delta A_\delta^{N-3} B_\delta & \cdots & C_\delta B_\delta \end{bmatrix} \in \mathbb{R}^{3N\times N},$$

$$\mathcal{T}_p = \begin{bmatrix} C_\delta F_\delta & 0 & 0 & \cdots & 0 \\ C_\delta A_\delta F_\delta & C_\delta F_\delta & 0 & \cdots & 0 \\ C_\delta A_\delta^2 F_\delta & C_\delta A_\delta F_\delta & C_\delta F_\delta & \cdots & 0 \\ \vdots & \vdots & \vdots & \ddots & \vdots \\ C_\delta A_\delta^{N-1} F_\delta & C_\delta A_\delta^{N-2} F_\delta & C_\delta A_\delta^{N-3} F_\delta & \cdots & C_\delta F_\delta \end{bmatrix} \in \mathbb{R}^{3N\times N}.$$

It is important to note that the increment prediction vector of the wave exciting force $\underline{\Delta f_{\text{ex}}}(k)$ in Eq. (16) is the input of the output prediction vector $\underline{Y}$ in Eq. (15). Therefore, determination of the optimal value of prediction horizon length N is essential, up to which the future wave exciting force must be predicted. Several methods have been proposed for predicting the wave exciting force $f_{\text{ex},\delta}$, including the extended Kalman filter (Nguyen and Tona, 2018; Li and Patton, 2023), and the impulse response function (Yoshimura et al., 2025). These prediction methods must be sufficiently fast and accurate to be compatible with the MPC controller design, thereby improving the feasibility of the optimization process. Otherwise, mismatches in the prediction model may reduce the MPC system's power-absorption performance, posing another challenge for MPC system development. Since our primary target is to determine the prediction horizon length N, the future wave exciting force $f_{\text{ex},\delta}$ is assumed to be provided throughout the specified prediction horizon length N. Consequently, the increment prediction vector of the wave exciting force $\underline{\Delta f_{\text{ex}}}$ is also considered to be known at any given time k. Although this simplifying assumption represents a limitation of the present study, the obtained optimal value of N provides useful insight into how far ahead the future wave exciting force should be incorporated into the MPC framework in Eq. (15).

iv. **Objective function**

The energy quantity absorbed by the PA-WEC, which is to be maximized across the time horizon $T_h = NT_s$, is given by

$$E_{t,t+T_h} = -\int_t^{t+T_h} f_{\text{PTO}}(\tau)\dot{\xi}(\tau)d\tau, \tag{18}$$

After applying the trapezoidal rule to numerically integrate Eq. (18), the objective function J can be approximated and derived by using the expression of the output prediction vector $\underline{Y}$ Eq. (15), as

$$J(k) = \frac{1}{2}\underline{Y}^{\text{T}}(k)Q\underline{Y}(k), \tag{19}$$

The matrix Q is given by

$$Q = \begin{bmatrix} U & & & \\ & \ddots & & \\ & & U & \\ & & & \frac{1}{2}U \end{bmatrix} \in \mathbb{R}^{3N\times 3N}, \text{ where } \quad U = \begin{bmatrix} 0 & 0 & 0 \\ 0 & 0 & 1 \\ 0 & 1 & 0 \end{bmatrix}.$$

By substituting Eq. (15) into Eq. (19), focusing only on the influence of the control force increment prediction vector $\underline{\Delta f_{\text{PTO}}}$ in the optimization process, the objective function J_1 to be minimized can be expressed as

$$J_1 = \frac{1}{2}\underline{\Delta f_{\text{PTO}}}^{\text{T}}\mathcal{T}_p^{\text{T}} Q \mathcal{T}_p \underline{\Delta f_{\text{PTO}}} + \underline{\Delta f_{\text{PTO}}}^{\text{T}}\mathcal{T}_p^{\text{T}} Q(\mathcal{T}_x x_\delta + \mathcal{T}_e \underline{\Delta f_{\text{ex}}}), \tag{20}$$

Eq. (20) indicates that the new objective function J_1 is a convex quadratic programming (CQP) problem, where the Hessian matrix is represented by $\mathcal{T}_p^{\text{T}} Q \mathcal{T}_p$, which is characterized as a positive semi-definite matrix. The objective function J_1 needs to be augmented with a penalty term to mitigate control aggressiveness, as suggested in Cretel et al. (2011). Accordingly, the objective function is modified as

$$J_2 = J_1 + \lambda_{\text{p}_1}\underline{\Delta f_{\text{PTO}}}^{\text{T}}\underline{\Delta f_{\text{PTO}}}, \tag{21}$$

Here, λ_{p_1} is introduced as a penalty term, which must be positive to maintain the convexity of the objective function, while its magnitude should remain sufficiently small to ensure that the objective functions J_1 and J_2 do not deviate significantly from each other. Consequently, this study defines the penalty term λ_{p_1} as the absolute value of the minimal eigenvalue of the Hessian matrix $\mathcal{T}_p^{\text{T}} Q \mathcal{T}_p$ as recommended in Sergiienko et al. (2021). The objective function J_2 needs to be further modified by incorporating an additional penalty term to reduce reactive power, which can lead to large instantaneous positive and negative powers in the PTO unit. This reversed power flow increases resistive and conversion losses. Therefore, to reduce these losses while maintaining the convexity of the objective function J_2, yielding the following modified expression:

$$J_3 = J_2 + \lambda_{\text{p}_2}\underline{f_{\text{PTO}}}^{\text{T}}\underline{f_{\text{PTO}}}, \tag{22}$$

where λ_{p_2} is the penalty term and the subsequent formulas are used to construct the objective function J_3, given by

$$\underline{f_{\text{PTO}}}(k) = L\underline{\Delta f_{\text{PTO}}}(k) + f_{\text{PTO},\delta}(k)I_u,$$

$$L = \begin{bmatrix} 1 & 0 & \cdots & 0 \\ 1 & 1 & \cdots & 0 \\ \vdots & \vdots & \ddots & \vdots \\ 1 & 1 & \cdots & 1 \end{bmatrix} \in \mathbb{R}^{N\times N}, \quad I_u = \begin{bmatrix} 1 \\ 1 \\ \vdots \\ 1 \end{bmatrix} \in \mathbb{R}^{N\times 1},$$

By combining the objective function expressions in Eqs. (20),(21) and (22), the final form of the objective function J_f can be written as

$$J_f(k) = \frac{1}{2}\underline{\Delta f_{\text{PTO}}}^{\text{T}}\Theta\underline{\Delta f_{\text{PTO}}} + \chi^{\text{T}}\underline{\Delta f_{\text{PTO}}}, \tag{23}$$

The following relations are used in the above expression of the objective function J_f

$$\Theta = \mathcal{T}_p^{\text{T}} Q \mathcal{T}_p + 2\lambda_{\text{p}_1}\mathbf{I} + 2\lambda_{\text{p}_2}L^{\text{T}}L,$$

$$\chi = \mathcal{T}_p^{\text{T}} Q(\mathcal{T}_x x_\delta(k) + \mathcal{T}_e\underline{\Delta f_{\text{ex}}}(k)) + 2\lambda_{\text{p}_2}L^{\text{T}}I_u f_{\text{PTO},\delta}(k).$$

To minimize the objective function given in Eq. (23), a CQP solver is used. After completing the optimization, the PA-WEC controller uses only the first component of the optimized PTO control force increment $\underline{\Delta f_{\text{PTO}}}$ at every time k, disregarding the following ones. Subsequently, the 4th-order Runge–Kutta method is employed to solve the motion equation of the floating body presented in Eq. (6) to determine the output state y_δ. At time $(k+1)$, the process will be repeated in a similar manner, using the previous optimal value as an initial guess. Fig. 2 illustrates the MPC framework for PA-WEC.

v. **Optimal prediction horizon length on regular waves**

The optimal prediction horizon length in MPC for the PA-WEC under regular wave conditions was investigated in the previous study (Kaiser et al., 2025). Accordingly, the present study adopts the empirical optimal solution of prediction horizon length N_{opt} derived in Kaiser et al. (2025), given by

$$N_{\text{opt}}T'_s = 2\pi\left(1 + \frac{2}{10\omega'}\right). \tag{24}$$

Here, $T'_s = T_s\sqrt{g/b}$ and $\omega' = \omega\sqrt{b/g}$ denote the nondimensional sampling interval and circular frequency, respectively, where b represents the half-breadth of the floating body.

The optimal solution Eq. (24) indicates that the optimal prediction horizon length is inversely proportional to the wave frequency, $N_{\text{opt}} \propto 1/\omega$, which implies that long waves require a long prediction horizon length, whereas a short prediction horizon length is sufficient for short waves. Additionally, it has been demonstrated in Kaiser et al. (2025) that MPC using the optimal prediction horizon length N_{opt} maximizes absorbed power and energy absorption efficiency, approaching the theoretical optimum, compared to the damping control method across all wave frequencies, especially at low frequencies. Since the computation time in MPC is significantly affected by the prediction horizon length

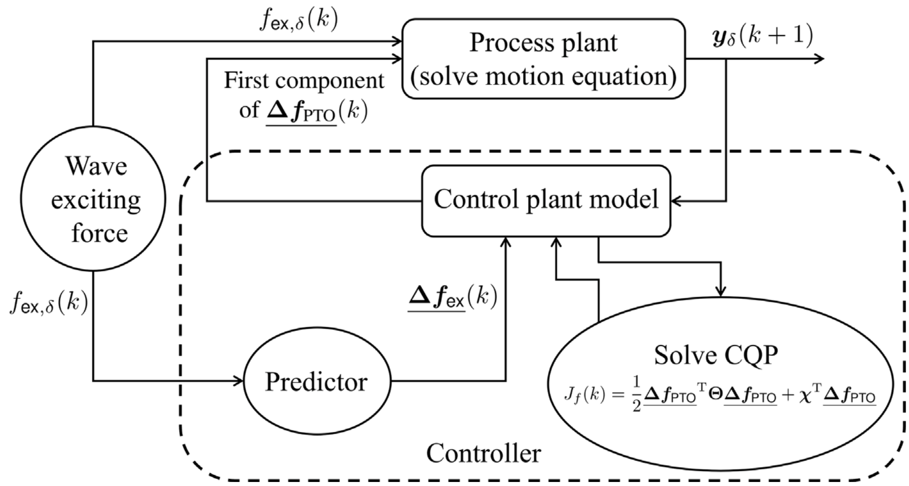

Fig. 2. Block diagram of the MPC framework for PA-WEC. The wave exciting force $f_{\mathrm{ex},\delta}(k)$ is provided to both the process plant and the predictor, where the predictor estimates the increments of wave exciting force $\underline{\boldsymbol{\Delta f}_{\mathrm{ex}}}(k)$. The CQP solver within the controller minimizes the objective function $J_f(k)$ to compute the optimal PTO force increment $\underline{\boldsymbol{\Delta f}_{\mathrm{PTO}}}$. Only the first component of $\underline{\boldsymbol{\Delta f}_{\mathrm{PTO}}}$ is applied to the process plant, which solves the motion equation to determine the output state $\boldsymbol{y}_\delta(k+1)$. At time $(k+1)$, the process will be repeated in a similar manner, using the previous optimal value as an initial guess.

N, the real-time factor (RTF), the ratio of the computation time to the sampling interval, is employed to assess the applicability of the optimal prediction horizon N_{opt} and determine its feasible range for real-time control. As shown in Kaiser et al. (2025), the proposed optimal prediction horizon length N_{opt} is applicable for real-time implementation over a wide range of frequencies, including low frequencies.

Based on these findings for the regular wave case in Kaiser et al. (2025), this study extends the investigation of the optimal prediction horizon length in MPC to irregular waves, maximizing energy absorption efficiency for sea state conditions. It should be noted that the sampling interval T_s also affects the performance of MPC. As discussed in Li et al. (2011), Kaiser et al. (2025), a sampling interval of $T_s = 0.1\,\mathrm{s}$ is reasonable considering the computational cost and real-time implementation. Therefore, throughout this paper, a consistent sampling interval of $T_s = 0.1\,\mathrm{s}$ is employed for all computations in the MPC formulation. Additionally, the penalty term $\lambda_{\mathrm{p}_2} = 2\,\mathrm{s}$ is set in all MPC simulations, which can eliminate the negative portion of the power cycle, consistent with the approach used in Kaiser et al. (2025).

2.3. Power and efficiency calculation

The primary objective of this study is to maximize the absorption power and energy absorption efficiency of a PA-WEC under irregular wave conditions. Since the linear superposition of regular waves results in irregular waves (Tobar Fuentes and Ledezma, 2024), and the linear superposition principle has been successfully applied for damping control (Murai and Iikura, 2020), whereby the absorbed power under irregular waves equals the sum of the absorbed powers associated with the regular wave components that constitute the irregular wave, the analysis of regular wave components is important. Therefore, this subsection first presents the absorption power and energy absorption efficiency for both the constant damping control method and MPC for a single wave component. Subsequently, following the superposition principle of absorbed power proposed in Murai and Iikura (2020), the applicability of the linear superposition principle is initially investigated for both constant damping control and MPC using two regular wave components. If the linear superposition principle holds for MPC in the two-wave components case, the analysis is then extended to irregular wave conditions for both control methods by investigating absorbed power and energy absorption efficiency.

2.3.1. Single regular wave

For a single regular wave with a frequency ω, the incident wave power P_W is given by

$$P_W = \frac{1}{2}\rho g \zeta^2 c_g = \frac{\rho g^2 \zeta^2}{4\omega}, \tag{25}$$

where c_g represents the group velocity, while the amplitude of the incident wave is referred to as ζ. It is important to note that the group velocity c_g is considered under the assumption of deep-water conditions.

The average absorbed power by the constant damping control force f_v for a single regular wave with frequency ω is derived as follows

$$P_{\mathrm{freq}}(\omega) = \frac{1}{T}\int_0^T v\dot{\xi}^2 dt = \frac{1}{2} v \omega^2 |\Xi|^2, \tag{26}$$

where T denotes the wave period. Using the relation in Eq. (9), the Eq. (26) can be rewritten as

$$P_{\mathrm{freq}}(\omega) = \frac{1}{2} v \omega^2 \frac{(\zeta F'_{\mathrm{ex}}(\omega)\rho g b)^2}{[-\omega^2\{m + A(\omega)\} + C_{\mathrm{s}}]^2 + \omega^2\{B(\omega) + v\}^2}, \tag{27}$$

Here, $F'_{\mathrm{ex}} = F_{\mathrm{ex}}/(\rho g \zeta b)$ represents the non-dimensional amplitude of the wave exciting force, which is obtained using the 2D-BEM. The energy absorption efficiency by the constant damping control η_{freq}, under regular wave conditions, can be formulated by dividing Eq. (27) by Eq. (25), as follows:

$$\eta_{\mathrm{freq}} = \frac{P_{\mathrm{freq}}}{P_W}. \tag{28}$$

Subsequently, the average absorbed power by the PTO unit under MPC for a single regular wave with a frequency ω, denoted by P_{MPC}, is expressed as

$$P_{\mathrm{MPC}}(\omega) = \frac{1}{T}\int_0^T P_{\mathrm{mech}}(t)dt = -\frac{1}{T}\int_0^T f_{\mathrm{PTO}}(t)\dot{\xi}(t)dt, \tag{29}$$

where P_{mech} represents the mechanical input power to the PA-WEC. Dividing Eq. (29) by Eq. (25), the energy absorption efficiency η_{MPC} by the PTO unit for a single regular wave is given by

$$\eta_{\mathrm{MPC}} = \frac{P_{\mathrm{MPC}}}{P_W}. \tag{30}$$

2.3.2. Two regular waves

Two regular wave components with distinct frequencies ω_a and ω_b are considered. According to the linear superposition theorem, the free surface elevation of an irregular incident wave formed by two corresponding regular wave components with the same incident wave amplitude ζ is constructed by

$$x_2(t) = \zeta \left\{ \cos(\omega_a t) + \cos(\omega_b t + \varepsilon) \right\}, \tag{31}$$

where ε is a random phase difference between the two components. The associated wave exciting force in the time domain is given by:

$$f_{\mathrm{ex}_2}(t) = \rho g b \zeta \left[F'_{\mathrm{ex}}(\omega_a)\cos(\omega_a t + \phi_a) + F'_{\mathrm{ex}}(\omega_b)\cos(\omega_b t + \phi_b + \varepsilon) \right], \tag{32}$$

Here, $F'_{\mathrm{ex}}(\omega_a)$ and $F'_{\mathrm{ex}}(\omega_b)$ denote the non-dimensional amplitudes, and ϕ_a and ϕ_b represent the phases of the wave exciting forces at frequencies ω_a and ω_b, respectively, and all of these values are obtained using the 2D-BEM.

The average absorbed powers at the frequencies ω_a and ω_b under constant damping control are denoted by $P_{\mathrm{freq,\ reg}}(\omega_a)$ and $P_{\mathrm{freq,\ reg}}(\omega_b)$, respectively, and are evaluated using Eq. (27). Following the computation of the displacement ξ, the average absorbed power P_{freq_2} for the superposition of two regular wave components under constant damping control force is evaluated using the expression provided in Eq. (26).

Under the assumptions of linear theory, the average absorbed power obtained using the damping control method for an irregular wave is equivalent to the summation of the average absorbed power associated with the corresponding regular wave components, as shown in Murai and Iikura (2020). This is referred to as the linear superposition principle and can be applied to the constant damping control method for two regular wave components, which yields the following relation

$$P_{\mathrm{freq,\ reg}}(\omega_a) + P_{\mathrm{freq,\ reg}}(\omega_b) = P_{\mathrm{freq}_2}. \tag{33}$$

Eq. (33) has two important implications. First, it enables validation of the computational accuracy of the absorbed power. Second, by summing the absorbed power associated with the regular-wave components, the absorbed power under irregular wave conditions can be readily determined. Based on these significances, this study investigates whether a similar linear superposition principle for absorbed power can be established for MPC, which can be expressed as

$$P_{\mathrm{MPC}}(\omega_a) + P_{\mathrm{MPC}}(\omega_b) = P_{\mathrm{MPC}_2}. \tag{34}$$

where $P_{\mathrm{MPC}}(\omega_a)$ and $P_{\mathrm{MPC}}(\omega_b)$ are the absorbed power computed using MPC at the individual frequencies ω_a and ω_b, respectively, and P_{MPC_2} denotes the absorbed power computed using MPC for the irregular wave formed by two regular wave components, as defined in Eq. (31). Following the validation of the linear superposition principle for absorbed power in MPC using two regular-wave components, a similar analysis is conducted for MPC under irregular wave conditions.

2.3.3. Irregular waves

The time series of a random incident wave can be generated, in a similar way, the superposition of two regular wave components described in Eq. (31), as follows:

$$x_{\mathrm{irr}}(t) = \sum_{i=1}^{I} \sqrt{2\Phi_{xx}(\omega_i)\Delta\omega_i}\cos(\omega_i t + \varepsilon_i), \tag{35}$$

Here, Φ_{xx} is the wave spectrum. The corresponding time series of the wave exciting force is obtained as

$$f_{\mathrm{ex,\ irr}}(t) = \rho g b \sum_{i=1}^{I} F'_{\mathrm{ex}}(\omega_i)\sqrt{2\,\Phi_{xx}(\omega_i)\,\Delta\omega_i}\,\cos(\omega_i t + \phi_i + \varepsilon_i), \tag{36}$$

Using the absorbed power relation given in Eq. (27), the average absorbed power for irregular waves at frequency ω_i, considering a constant damping control force, can be expressed as

$$\begin{aligned} P_{\mathrm{freq,\ irr}}(\omega_i) &= \frac{1}{2}\nu\,\omega_i^2 \frac{\left\{ \sqrt{2\,\Phi_{xx}(\omega_i)\,\Delta\omega_i}\,F'_{\mathrm{ex}}(\omega_i)\,\rho g b \right\}^2}{\left[-\omega_i^2\{m + A(\omega_i)\} + C_s \right]^2 + \omega_i^2\{B(\omega_i) + \nu\}^2} \\ &= \left\{ 2\,\Phi_{xx}(\omega_i)\,\Delta\omega_i \right\} P_{\mathrm{freq,\ reg}}(\omega_i), \end{aligned} \tag{37}$$

The average absorbed power $P_{\mathrm{freq,\ irr}}$ for irregular waves, based on the wave spectrum, considering a constant damping control force, can be determined as mentioned in Eq. (26).

To validate the control formulation based on the superposition principle as described in Eq. (33) for two regular wave components, the average absorbed power $P_{\mathrm{freq,\ irr}}$ under irregular waves should also be equal to the sum of the absorbed powers from each regular wave component that constitutes the wave spectrum shown in Eq. (37). This relationship is expressed as

$$P_{\mathrm{freq,\ irr}} = \sum_{i=1}^{I} P_{\mathrm{freq,\ irr}}(\omega_i) = \sum_{i=1}^{I} \{2\Phi_{xx}(\omega_i)\Delta\omega_i\} P_{\mathrm{freq,\ reg}}(\omega_i). \tag{38}$$

The incident wave power for irregular waves can be determined using either the spectrum or empirical wave parameters (Sierra et al., 2014), given below

$$P_{W,\ \mathrm{irr}} = \frac{\rho g^2}{2}\int_0^\infty \frac{\Phi_{xx}(\omega)}{\omega}d\omega = \frac{\rho g^2}{64\pi}H_s^2(0.86T_p), \tag{39}$$

where H_s and T_p represent the significant wave height and the peak period of the irregular waves, respectively. The energy absorption efficiency $\eta_{\mathrm{freq,\ irr}}$ for irregular waves under constant damping control force is expressed as

$$\eta_{\mathrm{freq,\ irr}} = \frac{P_{\mathrm{freq,\ irr}}}{P_{W,\ \mathrm{irr}}}. \tag{40}$$

The average absorbed power under irregular wave conditions using MPC, $P_{\mathrm{MPC,\ irr}}$, is given by

$$P_{\mathrm{MPC,\ irr}} = -\frac{1}{T}\int_0^T f_{\mathrm{PTO}}(t)\dot{\xi}(t)dt, \tag{41}$$

Subsequently, using the expression of average absorbed power under MPC control for a regular wave given in Eq. (29) and the superposition principle for constant damping control in Eq. (38), the applicability of linear superposition to the absorbed power under MPC can be expressed as

$$P_{\mathrm{MPC,\ irr}} = P_{\mathrm{MPC,\ reg,\ sum}} = \sum_{i=1}^{I} \{2\Phi_{xx}(\omega_i)\Delta\omega_i\} P_{\mathrm{MPC}}(\omega_i), \tag{42}$$

Here, $P_{\mathrm{MPC,\ reg,\ sum}}$ denotes the summation of the absorbed power obtained by applying the optimal solution given in Eq. (24) of MPC to each regular-wave component that comprises the irregular wave spectrum. The energy absorption efficiency $\eta_{\mathrm{MPC,\ irr}}$ of the MPC for irregular wave spectral conditions is defined by dividing Eq. (41) by Eq. (39), as

$$\eta_{\mathrm{MPC,\ irr}} = \frac{P_{\mathrm{MPC,\ irr}}}{P_{W,\ \mathrm{irr}}}, \tag{43}$$

The aggregated energy absorption efficiency $\eta_{\mathrm{MPC,\ reg,\ sum}}$, computed using the optimal solution of Eq. (24) for MPC by summing the efficiencies of individual regular wave components that constitute the irregular wave spectrum. The linear superposition principle for irregular waves will be analyzed to assess the applicability of the following relation for MPC:

$$\eta_{\mathrm{MPC,\ irr}} = \eta_{\mathrm{MPC,\ reg,\ sum}}. \tag{44}$$

3. Design

3.1. Generation of spectrum

For irregular wave analysis, the Albany wave energy development site in Western Australia is considered, located at 117.7547° E, 35.1081° S, with a water depth of 30 m and a mean annual wave power resource of 33.9 kW/m (Australian Renewable Energy Mapping Infrastructure, 2017). The site characteristics, the wave climate, and their representative sea states have been described in detail

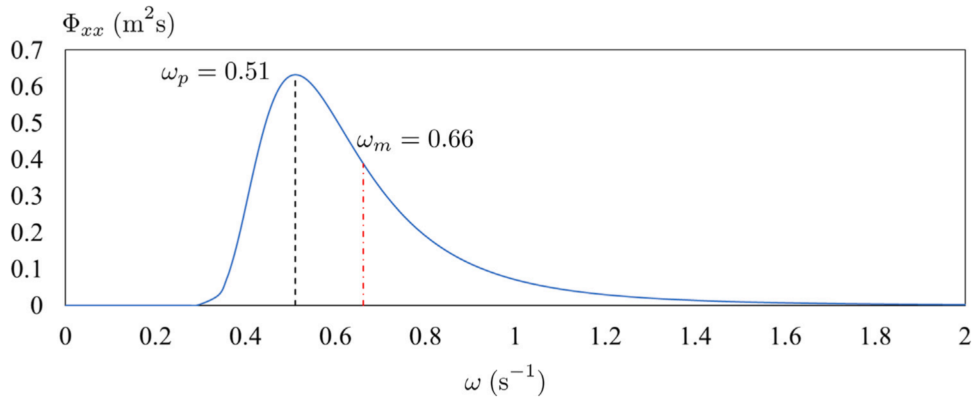

Fig. 3. Incident wave power spectrum is generated using the Pierson–Moskowitz spectrum, where the peak wave frequency $\omega_p = 0.51$ s^{-1} (black dashed line) and the mean wave frequency $\omega_m = 0.66$ s^{-1} (red dashed line).

in Sergiienko et al. (2021). All waves in sea states are assumed to be unidirectional, propagating in the positive x direction, ensuring consistency with the problem formulation as described in Fig. 1. The dimensions of the floating body are adjusted once for a given sea state to achieve maximum resonance under that condition. Therefore, the sea state with the highest probability of occurrence is selected for the analysis of energy absorption efficiency. Considering multiple sea states would require repeated adjustments to the floating body dimensions, significantly increasing the complexity of the analysis. The sea state with a peak wave period of $T_p = 12.3$ s and a significant wave height of $H_s = 1.9$ m is selected, as it exhibits the highest probability of occurrence (18.63%) among the sea states reported in Sergiienko et al. (2021). In the following subsection, the dimensions of the floating body are adjusted for this representative sea state. The mean wave period T_m can be determined from the peak wave period T_p using the following relation:

$$T_p = 1.296 T_m. \tag{45}$$

The Pierson–Moskowitz spectrum is employed to model irregular waves based on the significant wave height H_s and the mean wave period T_m. The corresponding incident wave spectrum in the frequency domain is given by

$$\Phi_{xx}(\omega) = \frac{A_s}{\omega^5} \exp\left\{-\frac{B_s}{\omega^4}\right\}, \tag{46}$$

where A_s and B_s are defined as

$$A_s = 172.8\,\frac{H_s^2}{T_m^4}, \quad B_s = \frac{691.2}{T_m^4}. \tag{47}$$

The wave spectrum Φ_{xx} is illustrated in Fig. 3 and characterized by a peak wave frequency of $\omega_p = 0.51$ s^{-1} and a mean wave frequency of $\omega_m = 0.66$ s^{-1}.

3.2. Adjustment of floating body dimensions

The dimensions of the floating body should be selected to obtain maximum resonance, ensuring maximum energy absorption efficiency for the specified wave spectrum illustrated in Fig. 3. As an initial approach, the dimensions of the floating body are adopted as a half-breadth of $b = 12.5$ m, corresponding to a half-breadth-to-draft ratio of $H_0 = 2.5$ following (Sergiienko et al., 2021), from which the sea state data are also obtained. This ensures the consistency of the problem formulation, providing a reliable reference under representative sea conditions. For maximum energy absorption efficiency, the dimension of the floating body needs to be adjusted such that the resonance frequency ω_r coincides with the peak wave frequency ω_p, which corresponds to the highest energy component of the wave spectrum. Additionally, tuning by peak frequency performs comparably across a range of frequencies (Hals et al., 2011), making it a more practical choice for heaving PA-WEC (Korde and Ertekin, 2015). The condition for resonance frequency is expressed as

$$C_s - \omega_r^2 (m + A) = 0. \tag{48}$$

The dimensions of the floating body are adjusted exclusively by varying the half-breadth b while maintaining the half-breadth-to-draft ratio H_0 constant. The investigation results reveal that when the half-breadth of the floating body is $b = 36$ m, the resonance frequency ω_r is almost perfectly aligned with the peak frequency ω_p, yielding a ratio of $\omega_r/\omega_p = 0.999$. For the floating body with a half-breadth $b = 36$ m, the amplitude ratio $\mathcal{A}$ between heave motion and wave exciting force for no control force and the energy absorption efficiency η for optimal damping control as a reference are determined in the frequency domain using the 2D-BEM, as described in Kaiser et al. (2025). Fig. 4 illustrates that for a half-breadth of $b = 36$ m, the amplitude ratio $\mathcal{A}$ and the energy absorption efficiency η reach maximum value at the peak wave frequency, indicating $\omega_r \approx \omega_p = 0.51$ s^{-1}. Therefore, the floating body with a half-breadth $b = 36$ m is identified as a potential candidate for the corresponding wave spectrum in Fig. 3 to achieve maximum energy absorption efficiency, and this floating body is used in the following subsections for analyzing the control methods.

4. Results

4.1. Validation of spectrum

The wave spectrum in Fig. 3 must be validated to ensure its accuracy before applying the irregular incident waves to the floating body for the control formulation. The Fourier transform is used to validate by reconstructing the spectrum of the incident wave time series in Eq. (35) into the frequency domain. The reconstructed spectrum is subsequently compared with the analytically defined spectrum in Eq. (46). The raw spectrum of the incident wave is obtained as

$$\Phi_{xx_r} = \frac{1}{2\pi^2} |X(\omega)|^2 \Delta\omega. \tag{49}$$

where $X(\omega)$ denotes the discrete Fourier transform (DFT) of the free-surface elevation time series $x_{\text{irr}}(t)$ in Eq. (35). This study employs the moving average (MA) method to smooth the raw spectrum Φ_{xx_r} with $p = 3$ points and iteratively applies it q times. The conditions for the MA method are shown in Appendix B.

Fig. 5 shows a comparison between the input spectrum Φ_{xx} and the smoothed spectrum Φ_{xx_r} of the incident waves for two cases of zero-upcrossing wave components: NW = 100 and NW = 400. It is worth noting that no window function is applied in this spectrum analysis, and all waves are generated using the same random number. In both cases, the smoothed spectrum shows good agreement with the input

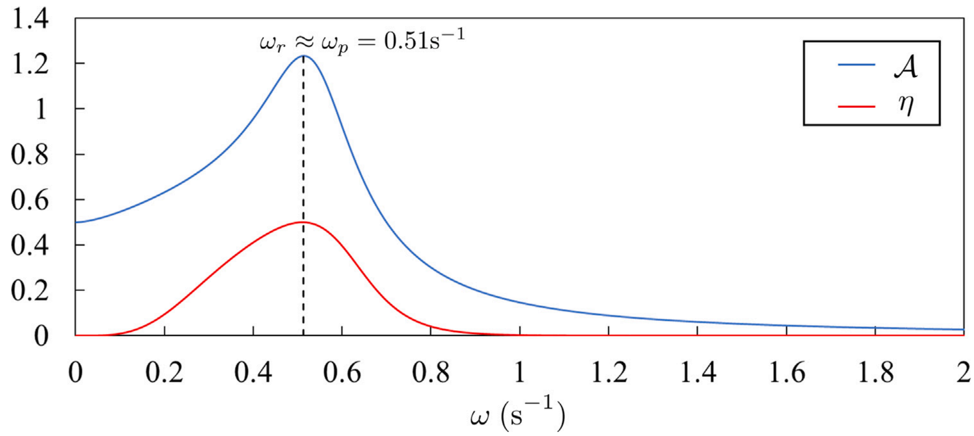

Fig. 4. Frequency response characteristics of the floating body, where the half-breadth is adjusted to $b = 36$ m, tuning the resonance frequency ω_r to coincide with the peak wave frequency ω_p. The amplitude ratio $\mathcal{A}$ represents the ratio between heave motion and wave exciting force, while η denotes the energy absorption efficiency; both reach their maximum values at the peak wave frequency ω_p.

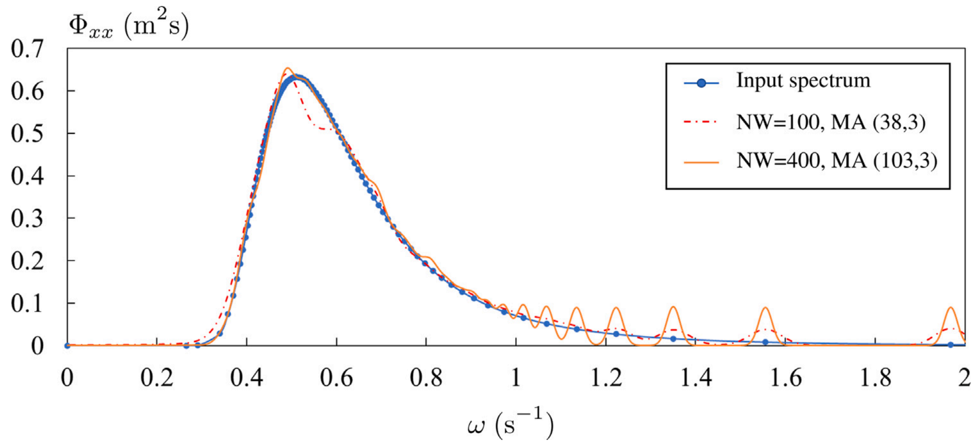

Fig. 5. Comparison of spectrum analysis between the analytically defined input spectrum and the smoothed spectrum of the incident waves for zero-upcrossing wave components: NW = 100 and NW = 400. Smoothing is performed by applying a moving average with $p = 3$ points, repeated q times. The values shown in parentheses of the legend represent the corresponding smoothing parameters (q, p).

spectrum. In particular, the smoothed spectrum obtained for NW = 400 shows better consistency with the input spectrum, thereby confirming the accuracy of the wave spectrum. However, the case with NW = 100 shows a slight discrepancy, particularly near the peak; nevertheless, the overall agreement remains satisfactory, validating the accuracy of the wave spectrum. Since the number of zero-upcrossing wave components NW = 100 is sufficient to represent the wave spectrum while reducing computational cost, NW = 100 is used for analyzing both control methods in the following Section 4.3 for irregular wave cases.

Validating the dynamic responses of floating bodies under no control force is crucial before implementing any control strategies. The response amplitude operators (RAOs) for the wave exciting force and the floating body's displacement are validated using the frequency and time domains and compared with results from 2D-BEM. Since the validation procedures for RAOs are comparable to those used for spectrum validation, the detailed procedures and results are shown in Appendix C.

4.2. Superposition of two regular waves

The linear superposition principle of absorption power has been demonstrated to be relevant to the damping control method (Murai and Iikura, 2020), and this study also evaluates its applicability to MPC. This subsection presents the results for the absorption power of both the constant damping control method and MPC for two regular wave components as a preliminary approach. Two regular wave components of equal amplitude $\zeta = 1$ m, with frequencies $\omega_a = 0.3$ s^{-1} and $\omega_b = 0.6$ s^{-1} are considered as an illustrative example in the vicinity of the peak wave frequency $\omega_p = 0.51$ s^{-1}.

4.2.1. Damping control

Table 1 provides a comparison of the absorbed power components using a constant damping control method where the damping coefficient $\nu = B(\omega_p)$ corresponds to the peak wave frequency ω_p. The first two rows show the average absorbed power corresponding to individual regular wave components with frequencies $\omega_a = 0.3\,\mathrm{s}^{-1}$ and $\omega_b = 0.6\,\mathrm{s}^{-1}$, denoted as $P_{\text{freq, reg}}(\omega_a)$ and $P_{\text{freq, reg}}(\omega_b)$, respectively. The third row shows the sum of these two values $P_{\text{freq, reg}}(\omega_a)+P_{\text{freq, reg}}(\omega_b)$, the average absorbed power expected from the linear superposition of the individual wave components. The fourth row presents the absorbed power P_{freq_2} directly calculated from the superposed wave input. Finally, the last row reveals the relative difference between the summed and superposed absorption powers, which is only 0.022%, indicating a high level of consistency and validating the principle of linear superposition as stated in Eq. (33) for the absorbed power under the given conditions. The absorbed power P_{freq_2} is compared with the corresponding results obtained using MPC in the following subsection.

4.2.2. MPC

Fig. 6 shows the average absorbed power obtained using MPC for different prediction horizon lengths N for the individual regular-wave

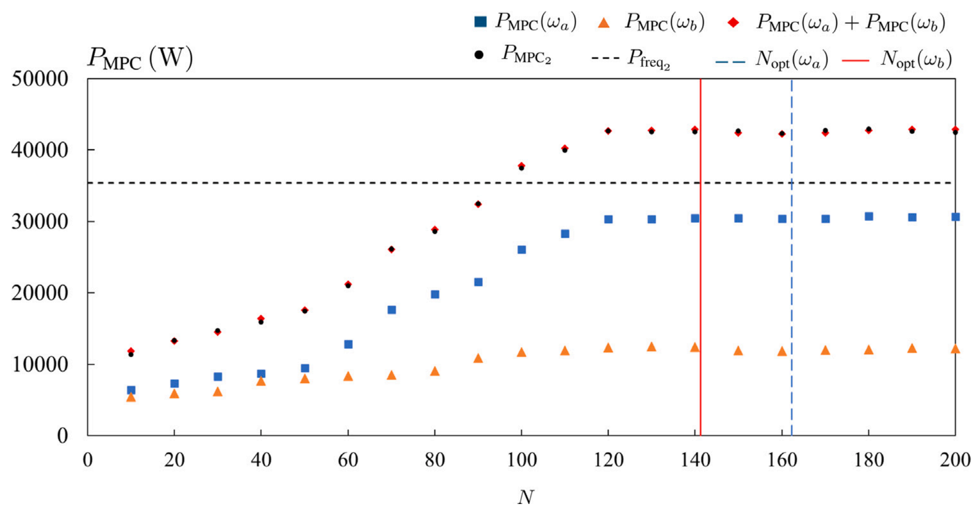

Fig. 6. Comparison of the average absorbed power for different prediction horizon lengths N under the MPC formulation. Results are presented for individual regular wave components at frequencies $\omega_a = 0.3\,\mathrm{s}^{-1}$ and $\omega_b = 0.6\,\mathrm{s}^{-1}$, as well as for their summation and superposition conditions. The corresponding values of the optimal prediction horizons are plotted as vertical lines: $N_{\mathrm{opt}}(\omega_a) = 162$ (long dashed blue) and $N_{\mathrm{opt}}(\omega_b) = 141$ (solid red). The dashed black line represents the absorbed power P_{freq_2} obtained using the constant damping control force.

Table 1
Comparison of absorbed power components under constant damping control force with $v = B(\omega_p)$ subjected to two regular wave components.

Component	Absorbed power (W)
$P_{\mathrm{freq,\ reg}}(\omega_a)$	18565.93
$P_{\mathrm{freq,\ reg}}(\omega_b)$	16784.22
$P_{\mathrm{freq,\ reg}}(\omega_a) + P_{\mathrm{freq,\ reg}}(\omega_b)$	35350.15
P_{freq_2}	35358.21
Relative difference	0.022%

components at frequencies $\omega_a = 0.3\,\mathrm{s}^{-1}$ and $\omega_b = 0.6\,\mathrm{s}^{-1}$, denoted as $P_{\mathrm{MPC}}(\omega_a)$ and $P_{\mathrm{MPC}}(\omega_b)$, respectively. Additionally, their linear summation, $P_{\mathrm{MPC}}(\omega_a) + P_{\mathrm{MPC}}(\omega_b)$ and the absorbed power obtained under the superposition of the two wave components, indicated by P_{MPC_2} are also plotted in Fig. 6.

The absorbed power of MPC for all cases in Fig. 6 increases with the extension of the prediction horizon length N. This trend gradually approaches a steady value, indicating convergence of the MPC performance. Since frequencies $\omega_a < \omega_b$ and shorter waves require a lower prediction horizon length N to reach steady values, the absorption power $P_{\mathrm{MPC}}(\omega_b)$ becomes stable at a relatively shorter prediction horizon length N compared to the absorption power $P_{\mathrm{MPC}}(\omega_a)$.

Notably, the superposition absorbed power P_{MPC_2} closely aligned with the linear summation $P_{\mathrm{MPC}}(\omega_a) + P_{\mathrm{MPC}}(\omega_b)$ for all prediction horizon lengths N. This agreement indicates that the linear superposition principle is applicable to MPC under linear theory for an irregular wave composed of two regular wave components, and the relation expressed in Eq. (34) is valid for MPC. The present MPC analysis is extended to the irregular wave spectrum in the following subsection.

The dashed black line in Fig. 6 indicates the absorbed power P_{freq_2} obtained by the constant damping control method corresponding to the constant damping coefficient at peak wave frequency ω_p as shown in Table 1. Beyond a prediction horizon length $N \geq 100$, MPC yields higher absorption power, $P_{\mathrm{MPC}_2} > P_{\mathrm{freq}_2}$ and consistently outperforms the constant damping control method for the superposition of two regular-wave components.

Based on the optimal solution of prediction horizon length N_{opt} for regular wave conditions in Eq. (24), the optimal prediction horizon lengths corresponding to the frequencies ω_a and ω_b, respectively, are defined by:

$$N_{\mathrm{opt}}(\omega_a)\, T_s' = 2\pi \left(1 + \frac{2}{10\omega_a'}\right), \tag{50}$$

$$N_{\mathrm{opt}}(\omega_b)\, T_s' = 2\pi \left(1 + \frac{2}{10\omega_b'}\right). \tag{51}$$

where ω_a' and ω_b' are the non-dimensional frequencies. The corresponding values of optimal prediction horizon length are illustrated in Fig. 6 as vertical lines: $N_{\mathrm{opt}}(\omega_a) = 162$ (long dashed blue) and $N_{\mathrm{opt}}(\omega_b) = 141$ (solid red), respectively. It can be observed that, for all cases, the average absorbed power computed using MPC converges before reaching the corresponding optimal prediction horizon lengths. In particular, the absorption power P_{MPC_2} attains its maximum value and remains consistent for $N \geq 120$ a range that is close to $N_{\mathrm{opt}}(\omega_b)$. This observation suggests that $N_{\mathrm{opt}}(\omega_b)$ can be considered as the optimal prediction horizon length for the superposition of two regular-wave components.

This finding confirms that when an irregular wave is formed with two different regular wave frequency components, the optimal prediction horizon length of MPC will be determined by substituting the higher frequency value into the optimal solution of prediction horizon length for the regular wave case in Eq. (24), which is sufficient for the maximum absorption power of MPC.

4.3. Irregular waves

The preceding Section 4.2 investigated the absorbed power for constant damping control and MPC, and demonstrated that the linear superposition principle is applicable for both control methods to an irregular wave composed of two regular wave components. Based on these results, this subsection further extends the analysis to irregular waves described by a wave spectrum, as introduced in Section 3.1. The absorbed power and corresponding energy absorption efficiency are evaluated under irregular wave conditions, and the applicability of the linear superposition principle to both control methods, especially MPC, is further examined. For both control methods, the time series of the wave exciting force $f_{\mathrm{ex,\ irr}}$ is generated using the expression Eq. (36), representing irregular waves as a linear superposition of multiple regular wave components with varying frequencies and random phases.

Table 2
Average absorbed power and energy absorption efficiency are computed using a constant damping coefficient for the case of $B(\omega_p)$ and $B(\omega_m)$ for irregular waves, compared with those obtained from the summation of regular wave components, and relative differences are computed accordingly.

Case	Wave type	$P_{\text{freq, irr}}$ (W)	$\eta_{\text{freq, irr}}$	Relative difference
$\nu = B(\omega_p)$	Summation of Regular Waves	6756.41	0.361	0.89%
	Irregular Waves	6696.95	0.358	
$\nu = B(\omega_m)$	Summation of Regular Waves	6140.72	0.328	0.91%
	Irregular Waves	6084.56	0.325	

4.3.1. Damping control

The performance of PA-WEC is influenced by wave frequency, with two specific frequencies in the wave spectrum being particularly significant. One is the peak wave frequency ω_p, which corresponds to the most energetic component of the wave spectrum. The other is the mean wave frequency ω_m, which governs the response amplification factor and thus determines the efficiency (Muraleedharan et al., 2023). Therefore, this study employs two cases for constant damping coefficient $\nu = B(\omega_p)$ and $\nu = B(\omega_m)$ to investigate the absorption performance of the constant damping control method under irregular wave conditions.

Table 2 presents the average absorbed power $P_{\text{freq, irr}}$ and energy absorption efficiency $\eta_{\text{freq, irr}}$ obtained using the constant damping control method. For the case of $\nu = B(\omega_p)$, the absorbed power of irregular waves is $P_{\text{freq, irr}} = 6696.95$ W, with an efficiency of $\eta_{\text{freq, irr}} = 0.358$, which closely aligns with the summation of regular wave components $P_{\text{freq, irr}} = 6756.41$ W and $\eta_{\text{freq, irr}} = 0.361$, respectively, resulting in a minimal relative difference of 0.89%. Despite this slight discrepancy, the overall results indicate that the superposition principle remains valid in estimating absorbed power under irregular wave conditions at $\nu = B(\omega_p)$.

In the following case, where $\nu = B(\omega_m)$, the absorbed power $P_{\text{freq, irr}} = 6084.56$ W and efficiency $\eta_{\text{freq, irr}} = 0.325$ also exhibit strong agreement with the summation of regular wave components respective results $P_{\text{freq, irr}} = 6140.72$ W and $\eta_{\text{freq, irr}} = 0.328$, showing a relative difference of only 0.91%. These results again confirm the applicability of the linear superposition principle and demonstrate the computational accuracy. Since the objective is to maximize energy absorption efficiency, and the constant damping control method yields higher efficiency for the case of $\nu = B(\omega_p)$, the corresponding absorbed power and efficiency, $P_{\text{freq, irr}} = 6696.95$ W and $\eta_{\text{freq, irr}} = 0.358$, respectively, are used for subsequent comparisons with the MPC strategy under irregular wave conditions.

4.3.2. MPC

The absorbed power $P_{\text{MPC, irr}}$ and energy absorption efficiency $\eta_{\text{MPC, irr}}$ obtained by the MPC formulation for irregular waves are shown in Figs. 7(a) and 7(b), respectively, evaluated over a range of prediction horizon lengths N. In both figures, the blue circular markers indicate the corresponding MPC-based absorbed power and energy absorption efficiency. It can be observed that the power $P_{\text{MPC, irr}}$ and efficiency $\eta_{\text{MPC, irr}}$ increase with the extension of the prediction horizon length N, reach a maximum value, and gradually approach a steady value, particularly for $N \geq 130$, indicating convergence of the MPC performance. Minor fluctuations in the power $P_{\text{MPC, irr}}$ and efficiency $\eta_{\text{MPC, irr}}$ are observed during convergence, which may arise from the uncertainty associated with irregular waves; however, these fluctuations are sufficiently small to be considered negligible.

The horizontal black dashed line in Figs. 7(a) and 7(b) indicates the power $P_{\text{freq, irr}} = 6696.95$ W and efficiency $\eta_{\text{freq, irr}} = 0.358$, respectively, obtained using constant damping control with a damping coefficient $\nu = B(\omega_p)$, given in Table 2 for irregular waves. As shown in Figs. 7(a) and 7(b), the power and efficiency obtained by the MPC formulation consistently exceed that of the constant damping control, i.e., $P_{\text{MPC, irr}} > P_{\text{freq, irr}}$, and $\eta_{\text{MPC, irr}} > \eta_{\text{freq, irr}}$, once the prediction horizon length reaches $N \gtrsim 90$, as indicated by the vertical blue dashed line in Fig. 7(b).

The red dash-dotted line in Figs. 7(a) and 7(b) denotes the aggregated absorbed power $P_{\text{MPC, reg, sum}} = 8769.86$ W and energy absorption efficiency $\eta_{\text{MPC, reg, sum}} = 0.467$ for MPC. These values are computed by applying the optimal solution of Eq. (24) to each constituent regular-wave component and summing their individual contributions to obtain the irregular wave spectrum. Both figures show that when the prediction horizon length $N \geq 130$, the power $P_{\text{MPC, irr}}$ and efficiency $\eta_{\text{MPC, irr}}$ become steady; they closely align with $P_{\text{MPC, reg, sum}}$ and $\eta_{\text{MPC, reg, sum}}$, respectively. This agreement indicates that the linear superposition principle is applicable to MPC under irregular wave conditions, and validates the relationships established for the absorbed power in Eq. (42) and the energy absorption efficiency in Eq. (44). It should be noted that the linear superposition principle in MPC may no longer hold under the following conditions:

- nonlinear hydrodynamic effects are introduced into the motion equation in Eq. (6)
- hard constraints become active, causing the explicit MPC control law to become piecewise affine in the system state (Bemporad et al., 2002)
- penalty terms introduce nonlinear dependence on the system states or control variables, resulting in a state-dependent Hessian matrix and transforming the QP into a nonlinear optimization problem (Guerrero-Fernandez et al., 2023)

Since the present study satisfies the assumptions required for the linear superposition principle, this principle can be employed to assess and validate the computational accuracy of the absorbed power and energy absorption efficiency obtained using the MPC formulation under irregular wave conditions.

For irregular wave conditions, the optimal solution of prediction horizon length in Eq. (24) is investigated by substituting the non-dimensional peak wave frequency ω'_p into the non-dimensional wave frequency ω', which results in the following empirical expression as

$$N_{\text{opt}}(\omega_p)\, T'_s = 2\pi \left(1 + \frac{2}{10\omega'_p}\right). \tag{52}$$

For the wave spectrum condition mentioned in Section 3.1, the optimal prediction horizon length is determined to be $N_{\text{opt}}(\omega_p) = 145$ and depicted by a vertical solid orange line in Fig. 7(b). The energy absorption efficiency obtained using the optimal prediction horizon length, $N_{\text{opt}}(\omega_p) = 145$, is $\eta_{\text{MPC, irr}} = 0.475$. This represents a 32.68% increase compared with the efficiency $\eta_{\text{freq, irr}} = 0.358$ obtained using the constant damping control method. Besides, it can be observed from Fig. 7(b) that, beyond the optimal line $N_{\text{opt}}(\omega_p)$, the energy absorption efficiency $\eta_{\text{MPC, irr}}$:

- maintains its maximum value and steady convergence.
- consistently exceeds the efficiency $\eta_{\text{freq, irr}}$ obtained from the constant damping control method.
- aligns closely with the summation of efficiency for regular wave components, thereby confirming the applicability of the linear superposition principle to MPC.

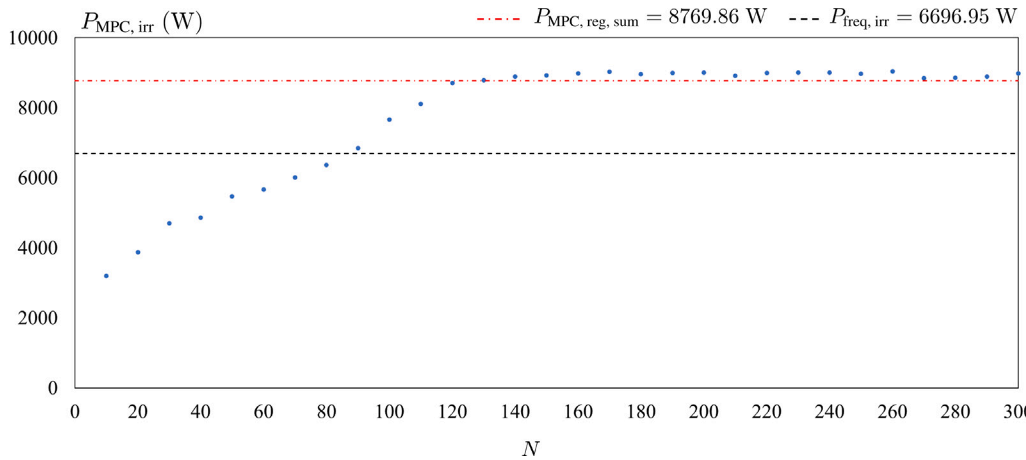

(a) Average absorbed power $P_{\mathrm{MPC,\ irr}}$

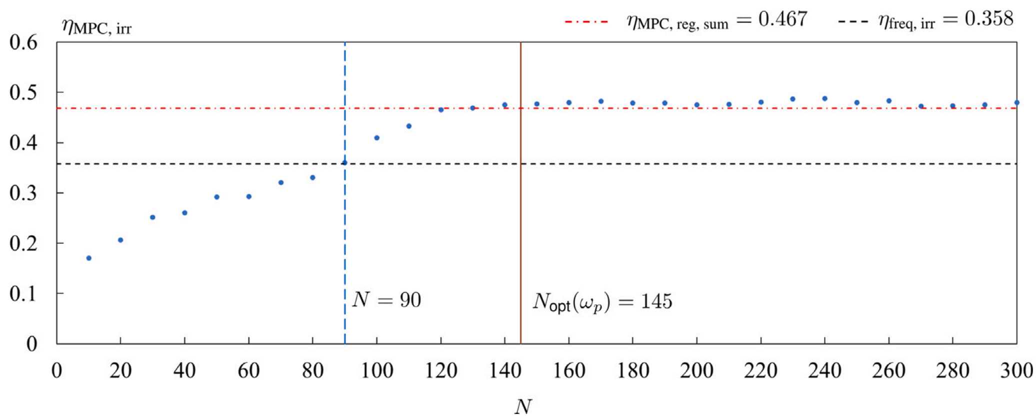

(b) Energy absorption efficiency $\eta_{\mathrm{MPC,\ irr}}$

Fig. 7. The MPC performances under irregular wave conditions are evaluated over varying prediction horizon lengths N. Subfigure (a) shows the average absorbed power $P_{\mathrm{MPC,\ irr}}$, indicated by blue circular markers. The horizontal red dash-dotted line and black dashed line denote the absorbed powers for $P_{\mathrm{MPC,\ reg,\ sum}}$ and $P_{\mathrm{freq,\ irr}}$ at $\nu = B(\omega_p)$, respectively. Subfigure (b) illustrates the corresponding energy absorption efficiency $\eta_{\mathrm{MPC,\ irr}}$ also marked by blue circular markers. The horizontal red dash-dotted and black dashed lines represent the efficiency values $\eta_{\mathrm{MPC,\ reg,\ sum}}$ and $\eta_{\mathrm{freq,\ irr}}$ at $\nu = B(\omega_p)$, respectively. The vertical solid orange line denotes the optimal prediction horizon $N_{\mathrm{opt}}(\omega_p) = 145$, determined based on the peak wave frequency ω_p.

A sensitivity analysis is conducted across ten different sea states at the Albany deployment site (Sergiienko et al., 2021) to investigate the generalizability of the proposed optimal prediction horizon length shown in Fig. 8. The floating-body half breadth, $b = 36$ m, is maintained in all cases, and the peak wave frequency ω_p varies from $\omega_p = 0.37$ to 0.67 s^{-1}. Fig. 8 demonstrates that the optimal prediction horizon length $N_{\mathrm{opt}}(\omega_p)$ decreases monotonically from 154 to 139 with the increase of ω_p, indicating that longer prediction horizon lengths are required for lower frequency sea states. The variation of $N_{\mathrm{opt}}(\omega_p)$ remains within a relatively narrow range, confirming the generalizability of the proposed optimal prediction horizon length.

Besides, the prediction horizon length N directly affects the computation time; therefore, the real-time feasibility of the optimal prediction horizon length $N_{\mathrm{opt}}(\omega_p)$ must be evaluated. The RTF increases quadratically with the time horizon (Kaiser et al., 2025), where it should be less than 1.0 to ensure real-time feasibility. In this study, all computations are performed on a desktop computer featuring a 2.90 GHz CPU and 16 GB RAM (15.8 GB available). Fig. 9 shows the RTF with respect to the time horizon NT_s s with a sampling interval of $T_s = 0.1$ s. The black dashed horizontal line represents RTF = 1.0. The vertical solid orange line indicates the optimal time horizon, $N_{\mathrm{opt}}(\omega_p)T_s = 14.5$ s, corresponding to the optimal prediction horizon length $N_{\mathrm{opt}}(\omega_p) = 145$. It can be observed that the RTF corresponding to $N_{\mathrm{opt}}(\omega_p)$ remains below 1.0, and when the time horizon $NT_s \gtrsim 19$ s,

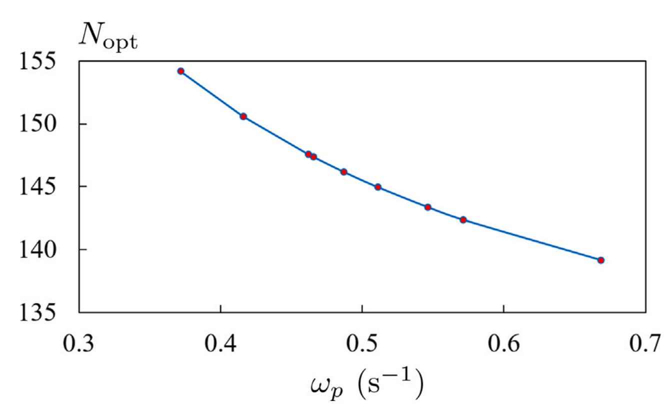

Fig. 8. Sensitivity of the optimal prediction horizon length $N_{\mathrm{opt}}(\omega_p)$ to ten different sea states at the Albany deployment site (Sergiienko et al., 2021). The floating-body half breadth, $b = 36$ m, is maintained in all cases, and the peak wave frequency ω_p varies from $\omega_p = 0.37$ to 0.67 s^{-1}. The optimal prediction horizon length $N_{\mathrm{opt}}(\omega_p)$ decreases monotonically from 154 to 139 with the increase of ω_p.

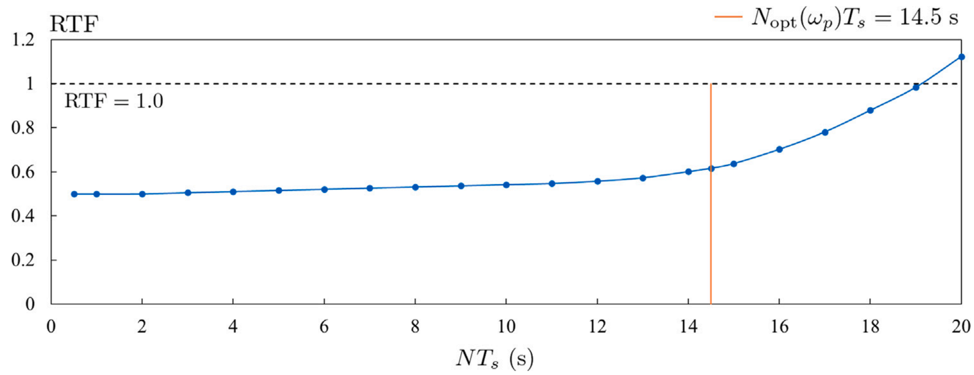

Fig. 9. Real-time factor (RTF) for different values of the time horizon NT_s. The black dashed horizontal line indicates RTF = 1.0. The vertical solid orange line denotes the optimal time horizon $N_{\text{opt}}(\omega_p)T_s = 14.5$ s, corresponding to optimal prediction horizon length $N_{\text{opt}}(\omega_p) = 145$ and sampling interval $T_s = 0.1$ s.

Table 3
Comparison of MPC (using prediction horizon length $N_{\text{opt}}(\omega_p) = 145$) and constant damping control with a damping coefficient $\nu = B(\omega_p)$ in terms of absorbed power, energy absorption efficiency, and computational requirements under irregular wave conditions.

Performance	MPC	Constant damping control
Absorbed power	8892.82 W	6696.95 W
Energy absorption efficiency	0.475	0.358
Future wave exciting force	Required (up to 14.5 s ahead)	Not required
Optimization	CQP solved at each sampling interval T_s	Not required
Real-time feasibility	Feasible (RTF < 1.0 at N_{opt})	Always feasible
Computational requirement	Higher	Lower

the RTF becomes greater than 1.0, which is not acceptable for real-time formulation. Thereby confirming that the proposed optimal prediction horizon length $N_{\text{opt}}(\omega_p)$ is feasible for real-time implementation. It is worth noting that the time horizon condition $NT_s \gtrsim 19$ s depends on the computational capability of the device. Computation with a longer prediction length can be performed in real time by employing a more powerful device. Nevertheless, even under such conditions, the proposed optimal prediction horizon would still remain more efficient due to its lower computational demand.

Therefore, all of the abovementioned findings confirm that the optimal prediction horizon length $N_{\text{opt}}(\omega_p)$, derived based on the peak wave frequency ω_p of the wave spectrum, is suitable for MPC to maximize energy absorption efficiency for irregular wave analysis in real-time. Consequently, for any given wave spectrum, $N_{\text{opt}}(\omega_p)$ enables the determination of how far in advance the prediction of future wave exciting forces is required. Table 3 summarizes the comparison between MPC (results obtained by prediction horizon length $N_{\text{opt}}(\omega_p) = 145$) and constant damping control with a damping coefficient $\nu = B(\omega_p)$ in terms of absorbed power, energy absorption efficiency, and computational requirements under irregular wave conditions.

In this study, under the specified spectral condition described in Section 3.1, the optimal prediction horizon length $N_{\text{opt}}(\omega_p) = 145$ and sampling interval $T_s = 0.1$ s, which leads to the time horizon of $T_h = 14.5$ s. This observation leads to the conclusion that, for the real-time implementation of MPC under the specified wave conditions, predicting the future wave exciting force approximately 14.5 s in advance is sufficient to maximize the energy absorption performance of the PA-WEC for a floating body with a half breadth $b = 36$ m.

4.4. Practical implementation challenges for offshore deployment

Real offshore deployment of MPC for PA-WEC introduces several practical challenges. Since the optimal solution for the prediction horizon length determines how far in advance the future wave exciting force must be predicted, the wave prediction model must be sufficiently fast and accurate to complete computations within the prediction horizon length at each sampling interval. Therefore, to ensure real-time computational feasibility and to address computational loads, computationally capable hardware is required. Another issue is that although the linear hydrodynamic model provides a computationally efficient approach for MPC formulation (Ringwood et al., 2014), WEC systems will encounter nonlinear effects in real sea conditions. Under such conditions, both model mismatch and real-time prediction of exciting forces can reduce the MPC power gain relative to idealized simulations (Hillis et al., 2020). Addressing the non-linear effect in the problem formulation is our future work. Additionally, the PTO system is not ideal in real applications; in such cases, the nonlinear efficiency depends on the energy flow direction (Guerrero-Fernandez et al., 2023). Beyond these challenges, hardware failures, sensor malfunctions, and limited access for maintenance can occur during real offshore deployment of the WEC system (Kelly et al., 2014).

5. Conclusions

This study proposes an optimal prediction horizon length for MPC to maximize the energy absorption efficiency of a PA-WEC, which defines the time frame over which the wave exciting force must be predicted for real-time control under irregular sea conditions. The dimensions of the floating body of PA-WEC are tuned according to the sea state. The performance of MPC is compared with that of constant damping control as a reference. Irregular waves are generated in two ways: by the superposition of two regular waves and by a wave spectrum. For both cases, the linear superposition principle is investigated in both control methods. Under linear theory, the results confirm the applicability of the linear superposition principle to both control methods, especially MPC. Additionally, the MPC method consistently demonstrates superior absorption capability and energy absorption efficiency compared to constant damping control under all conditions. For an irregular wave formed by the superposition of two regular waves, the optimal prediction horizon length in MPC is determined by substituting the higher frequency component into the optimal solution of the prediction horizon relation obtained for the regular wave case. In contrast, for irregular waves characterized by a wave spectrum, the optimal prediction horizon length is determined by substituting the peak frequency

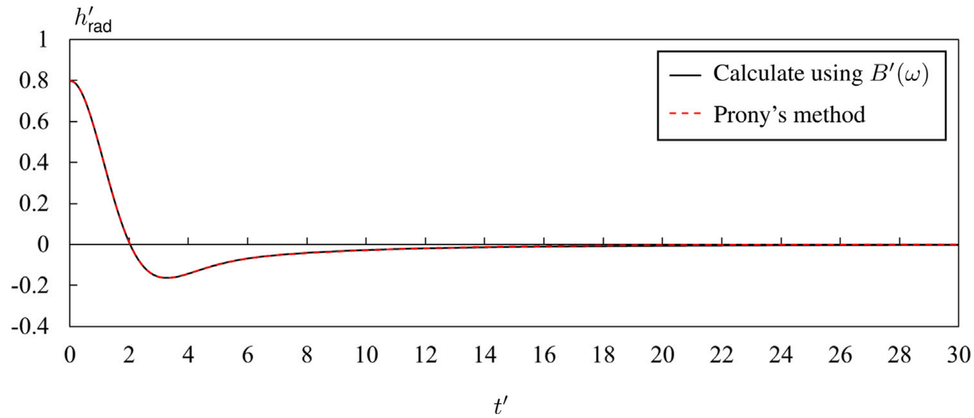

Fig. A.10. Non-dimensional radiation impulse function h'_{rad} is obtained by integrating the normalized damping coefficient $B'(\omega)$ and approximated using Prony's method with an order of $n = 10$.

of the spectrum into the empirical relation derived under regular wave conditions. Based on the given spectrum with a peak wave frequency of $\omega_p = 0.51\,\mathrm{s}^{-1}$, the corresponding optimal prediction horizon length is determined as $N_{\mathrm{opt}}(\omega_p) = 145$. The efficiency obtained using the optimal prediction horizon length, $N_{\mathrm{opt}}(\omega_p)$, is 32.68% higher than the constant damping control method. Considering the sampling interval $T_s = 0.1\,\mathrm{s}$, the time horizon becomes $T_h = 14.5\,\mathrm{s}$. Consequently, under the given spectral conditions, the wave exciting force must be predicted 14.5 s in advance for the real-time implementation of MPC to maximize energy absorption performance by a PA-WEC for a floating body with a half breadth $b = 36\,\mathrm{m}$.

It is worth noting that the linear superposition principle in this study is applicable under linear theory. Its applicability may no longer hold when nonlinear effects are introduced into the equation of motion, when hard constraints become active, or when penalty terms introduce nonlinear dependence on system states or control variables. Therefore, the applicability of the linear superposition principle under nonlinear hydrodynamic conditions will be investigated in future work.

CRediT authorship contribution statement

Md Shahidullah Kaiser: Writing – original draft, Visualization, Validation, Software, Resources, Methodology, Investigation, Formal analysis. **Takahito Iida:** Writing – original draft, Supervision, Resources, Project administration, Funding acquisition, Data curation, Conceptualization. **Ryo Yoshimura:** Writing – review & editing, Software, Resources, Investigation.

Declaration of competing interest

The authors declare the following financial interests/personal relationships which may be considered as potential competing interests: Takahito Iida reports financial support was provided by Japan Society for the Promotion of Science. If there are other authors, they declare that they have no known competing financial interests or personal relationships that could have appeared to influence the work reported in this paper.

Acknowledgment

JSPS KAKENHI Grant Number JP23K13504 supported this work.

Appendix A. Radiation impulse response function

Fig. A.10 demonstrates the non-dimensional radiation impulse response function $h'_{\mathrm{rad}} = h_{\mathrm{rad}}/\rho g b$, which is obtained using Eq. (4) by integrating the non-dimensional damping coefficient $B' = B/\rho\omega b^2$, and subsequently approximated using Prony's method with an order of $n = 10$. It can be observed that they show good agreement with each other, indicating that $n = 10$ is sufficient for convergence.

Appendix B. Moving average method

The conditions for the MA method are given by

$$\begin{cases} v_1 &= \Phi_{xx_r}(\omega_i) - \Phi_{xx_r}(\omega_{i-1}), \\ v_2 &= \Phi_{xx_r}(\omega_{i+1}) - \Phi_{xx_r}(\omega_i), \\ v_1 &> 0 \quad \text{and} \quad v_2 < 0 \quad \text{and} \quad \Phi_{xx_r}(\omega_i) > 0.1 \quad \text{and} \quad \omega_i < \omega_{\max}. \end{cases} \tag{B.1}$$

When there is only one frequency ω that satisfies the above condition (B.1) within the interval $[\omega_{\min}, \omega_{\max}]$, the smoothing procedure is terminated, which indicates that there exists only a single peak in this range. However, attempting to eliminate the peak toward the right end may result in excessive smoothing. Therefore, only peaks that exceed an appropriate threshold of 0.1 or greater are considered.

Appendix C. Validation of RAO

This section validates the response amplitude operators (RAOs) of the wave exciting force and the displacement of the proposed floating body with a half-breadth of $b = 36\,\mathrm{m}$ under no control force. Based on the time series of the wave exciting force described in Eq. (36), the raw spectrum of the wave exciting force is computed as

$$\Phi_{yy} = \frac{1}{2\pi^2}|F_{\mathrm{ex}}(\omega)|^2 \Delta\omega, \tag{C.1}$$

Using the raw spectrums of the wave exciting force Φ_{yy} and the incident wave Φ_{xx_r}, the amplitude of the wave exciting force $|F_{\mathrm{ex}}|$ is obtained by

$$|F_{\mathrm{ex}}| = \sqrt{\frac{\Phi_{yy}}{\Phi_{xx_r}}}, \tag{C.2}$$

The cross-spectrum of the wave exciting force with respect to the incident wave is written as

$$\Phi_{yx} = \frac{1}{2\pi^2} F_{\mathrm{ex}}(\omega)\overline{X(\omega)}\Delta\omega, \tag{C.3}$$

Here, $\overline{X(\omega)}$ is the complex conjugate of the Fourier transform of the incident wave. Using the cross-spectrum of the wave exciting force Φ_{yx}, the phase of the wave exciting force is determined as the argument (phase angle) of the cross-spectrum of the wave exciting force as follows:

$$\arg(F_{\mathrm{ex}}) = \arg(\Phi_{yx}). \tag{C.4}$$

Figs. C.11(a) and C.11(b) demonstrate the comparison of the amplitude and the phase of the wave exciting force, respectively. The results include the smoothed data obtained using the MA method mentioned in Eq. (B.1) and are compared with those computed by the 2D-BEM. As observed from Figs. C.11(a) and C.11(b), the smoothed data are consistent

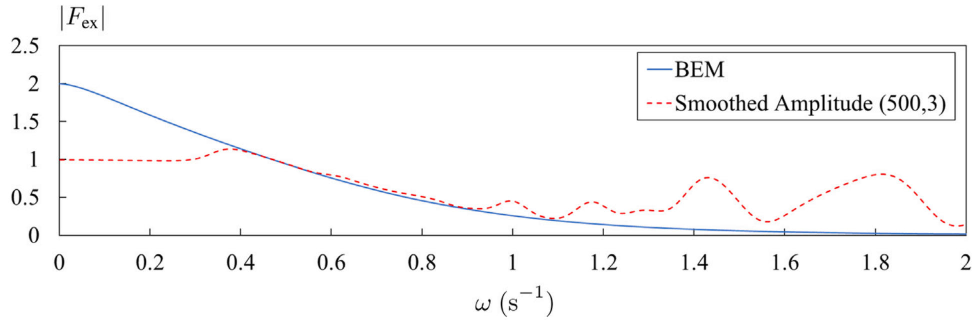

(a) Amplitude of wave exciting force

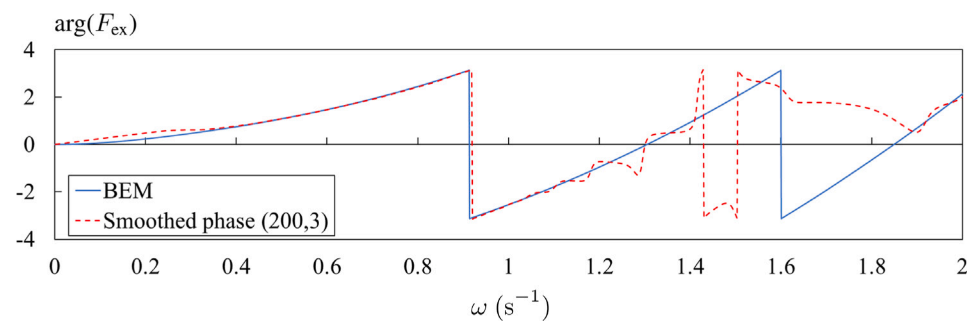

(b) Phase of wave exciting force

Fig. C.11. Comparison of (a) the amplitude and (b) the phase of the wave exciting force for the floating body $b = 36$ m. Results are presented for the smoothed data obtained using the MA method, and are compared with those computed by the 2D-BEM.

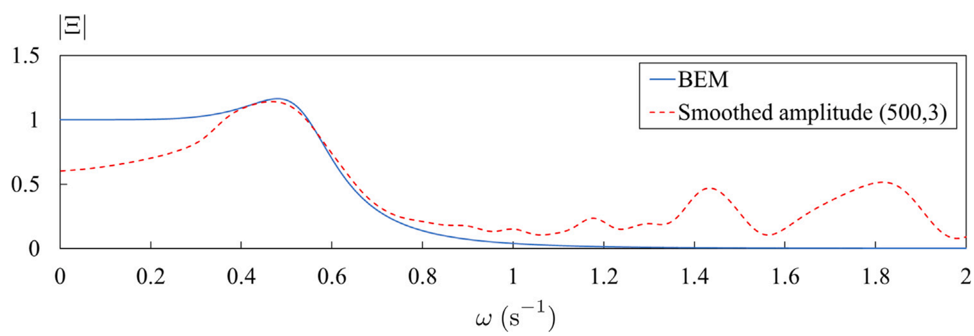

(a) Amplitude of motion

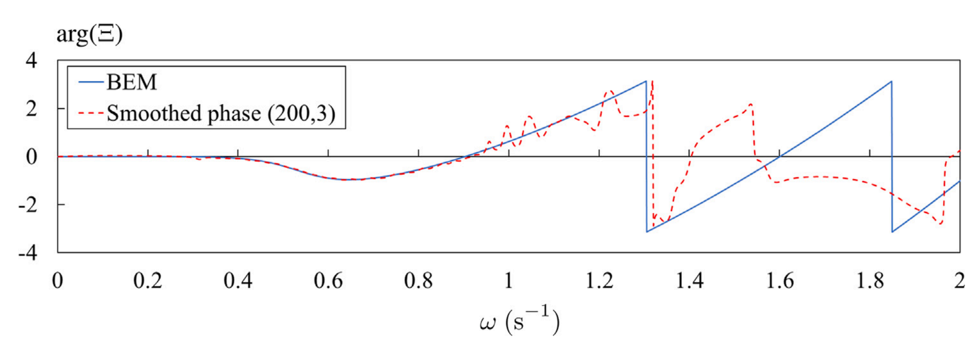

(b) Phase of motion

Fig. C.12. Comparison of (a) the amplitude and (b) the phase of the heave motion for the floating body $b = 36$ m under no control force. Results are presented for the smoothed data obtained using the MA method, and are compared with those computed by the 2D-BEM.

with the BEM over a wide frequency range. However, the agreement deteriorates rapidly in regions such as low and high frequencies, where no raw data are available in the incident-wave power spectrum. In contrast, the BEM result is smooth and physically consistent. Therefore, despite these discrepancies, the BEM validates the amplitude and phase of the wave exciting force obtained from the spectrum analysis.

The time series of heave motion $\xi(t)$ can be determined by solving the equation of motion Eq. (6) under no control force. The amplitude and phase of the heave motion can be obtained in the same manner as the amplitude and phase of the wave exciting force, as mentioned in Eqs. (C.2) and (C.4). The amplitude of the heave motion $|\Xi|$ can be expressed as

$$|\Xi| = \sqrt{\frac{\Phi_{zz}}{\Phi_{xx_r}}}, \tag{C.5}$$

where Φ_{zz} is the raw spectrum of the heave motion under no control force. The phase of the motion can be written as

$$\arg(\Xi) = \arg(\Phi_{yz}). \tag{C.6}$$

Here, Φ_{yz} is the cross-spectrum of the motion with respect to the incident wave.

Figs. C.12(a) and C.12(b) show the comparison of the amplitude and the phase of the heave motion, respectively, under no control force. The comparison results include the smoothed data obtained using the MA method, which are consistent with the 2D-BEM results. However, notable numerical discrepancies occur at both low and high frequencies, for reasons similar to those previously identified during validation of the wave exciting force, and do not affect the validation criteria. Therefore, the overall agreement confirms that the BEM results validate the motion amplitude and phase obtained from the spectrum analysis.

Data availability

On reasonable request, data will be made available.

References

Afram, A., Janabi-Sharifi, F., 2014. Theory and applications of HVAC control systems – a review of model predictive control (MPC). Build. Environ. 72, 343–355. http://dx.doi.org/10.1016/j.buildenv.2013.11.016, URL https://www.sciencedirect.com/science/article/pii/S0360132313003363.

Alkhatib, I.I., Garlisi, C., Pagliaro, M., Al-Ali, K., Palmisano, G., 2020. Metal-organic frameworks for photocatalytic CO2 reduction under visible radiation: A review of strategies and applications. Catal. Today 340, 209–224. http://dx.doi.org/10.1016/j.cattod.2018.09.032, URL https://www.sciencedirect.com/science/article/pii/S0920586118305984, SI: Advance in Photocatalysis.

Australian Renewable Energy Mapping Infrastructure, 2017. Australian Wave Energy Atlas. (Accessed 24 October 2017), http://nationalmap.gov.au/renewables/.

Babarit, A., Clément, A., 2006. Optimal latching control of a wave energy device in regular and irregular waves. Appl. Ocean Res. 28 (2), 77–91. http://dx.doi.org/10.1016/j.apor.2006.05.002.

Babarit, A., Guglielmi, M., Clément, A.H., 2009. Declutching control of a wave energy converter. Ocean Eng. 36 (12), 1015–1024. http://dx.doi.org/10.1016/j.oceaneng.2009.05.006, URL https://www.sciencedirect.com/science/article/pii/S0029801809001115.

Bemporad, A., Morari, M., Dua, V., Pistikopoulos, E.N., 2002. The explicit linear quadratic regulator for constrained systems. Automatica 38 (1), 3–20. http://dx.doi.org/10.1016/S0005-1098(01)00174-1, URL https://www.sciencedirect.com/science/article/pii/S0005109801001741.

Bertsekas, D., 1995. Dynamic programming and optimal control. In: Athena Scientific optimization and computation series, (v. 1), Athena Scientific.

Bøhn, E., Gros, S., Moe, S., Johansen, T.A., 2021. Reinforcement learning of the prediction horizon in model predictive control. IFAC-PapersOnLine 54 (6), 314–320. http://dx.doi.org/10.1016/j.ifacol.2021.08.563, 7th IFAC Conference on Nonlinear Model Predictive Control NMPC 2021.

Brekken, T.K., 2011. On model predictive control for a point absorber wave energy converter. In: 2011 IEEE Trondheim PowerTech. pp. 1–8. http://dx.doi.org/10.1109/PTC.2011.6019367.

Coe, R.G., Bacelli, G., Wilson, D.G., Abdelkhalik, O., Korde, U.A., Robinett III, R.D., 2017. A comparison of control strategies for wave energy converters. Int. J. Mar. Energy 20, 45–63. http://dx.doi.org/10.1016/j.ijome.2017.11.001.

Cretel, J., Lightbody, G., Thomas, G., Lewis, A., 2011. Maximisation of energy capture by a wave-energy point absorber using model predictive control. IFAC Proc. Vol. 44 (1), 3714–3721. http://dx.doi.org/10.3182/20110828-6-IT-1002.03255, 18th IFAC World Congress.

Cummins, W.E., 1962. The impulse response function and ship motion. Report 1661, Department of the Navy, David W. Taylor Model Basin, Hydromechanics Laboratory, Research and Development Report.

Duclos, G., Clément, A.H., Chatry, G., 2000. Absorption of outgoing waves in a numerical wave tank using a self-adaptive boundary condition. Int. J. Offshore Polar Eng. 11, 185–192.

Eidsmoen, H., 1998. Tight-moored amplitude-limited heaving-buoy wave-energy converter with phase control. Appl. Ocean Res. 20 (3), 157–161. http://dx.doi.org/10.1016/S0141-1187(98)00013-3.

Evans, D., 1981. Maximum wave-power absorption under motion constraints. Appl. Ocean Res. 3 (4), 200–203. http://dx.doi.org/10.1016/0141-1187(81)90063-8.

Falnes, J., 2002. Ocean Waves and Oscillating Systems: Linear Interactions Including Wave-Energy Extraction. Cambridge University Press.

Fusco, F., Ringwood, J.V., 2013. A simple and effective real-time controller for wave energy converters. IEEE Trans. Sustain. Energy 4 (1), 21–30. http://dx.doi.org/10.1109/TSTE.2012.2196717.

Gao, H., Xiao, J., 2021. Effects of power take-off parameters and harvester shape on wave energy extraction and output of a hydraulic conversion system. Appl. Energy 299, 117278. http://dx.doi.org/10.1016/j.apenergy.2021.117278, URL https://www.sciencedirect.com/science/article/pii/S0306261921006954.

Genest, R., Ringwood, J., 2016. A critical comparison of model-predictive and pseudospectral control for wave energy devices. J. Ocean. Eng. Mar. Energy 2, http://dx.doi.org/10.1007/s40722-016-0058-2.

Guerrero-Fernandez, J.L., González-Villarreal, O.J., Rossiter, J.A., 2023. Efficiency-aware nonlinear model-predictive control with real-time iteration scheme for wave energy converters. Internat. J. Control 96 (8), 1909–1921. http://dx.doi.org/10.1080/00207179.2022.2078424.

Hals, J., Falnes, J., Moan, T., 2010a. Constrained optimal control of a heaving buoy wave-energy converter. J. Offshore Mech. Arct. Eng. 133 (1), 011401. http://dx.doi.org/10.1115/1.4001431, arXiv:https://asmedigitalcollection.asme.org/offshoremechanics/article-pdf/133/1/011401/5931345/011401_1.pdf.

Hals, J., Falnes, J., Moan, T., 2010b. Constrained optimal control of a heaving buoy wave-energy converter. J. Offshore Mech. Arct. Eng. 133 (1), 011401. http://dx.doi.org/10.1115/1.4001431.

Hals, J., Falnes, J., Moan, T., 2011. A comparison of selected strategies for adaptive control of wave energy converters. J. Offshore Mech. Arct. Eng. 133 (3), 031101. http://dx.doi.org/10.1115/1.4002735, arXiv:https://asmedigitalcollection.asme.org/offshoremechanics/article-pdf/133/3/031101/5564608/031101_1.pdf.

Han, M., Cao, F., Shi, H., Kou, H., Gong, H., Wang, C., 2023. Parametrical study on an array of point absorber wave energy converters. Ocean Eng. 272, 113857. http://dx.doi.org/10.1016/j.oceaneng.2023.113857, URL https://www.sciencedirect.com/science/article/pii/S002980182300241X.

Hernández-Robles, I.A., González-Ramírez, X., Gómez-Gutiérrez, J.A., Ramirez, J.M., 2021. Wave power assessment for electricity generation with powerbouy system by wave motion emulation modelling. Sustain. Energy Technol. Assessments 43, 100962. http://dx.doi.org/10.1016/j.seta.2020.100962, URL https://www.sciencedirect.com/science/article/pii/S2213138820313904.

Hillis, A., Yardley, J., Plummer, A., Brask, A., 2020. Model predictive control of a multi-degree-of-freedom wave energy converter with model mismatch and prediction errors. Ocean Eng. 212, 107724. http://dx.doi.org/10.1016/j.oceaneng.2020.107724.

Holthuijsen, L.H., 2007. Waves in Oceanic and Coastal Waters. Cambridge University Press.

Iida, T., Minoura, M., 2022. Analytical solution of impulse response function of finite-depth water waves. Ocean Eng. 249, 110862. http://dx.doi.org/10.1016/j.oceaneng.2022.110862.

Jama, M., Wahyudie, A., Assi, A., Noura, H., 2014. Function-based model predictive control approach for maximum power capture of heaving wave energy converters. In: Hamdan, M.O., Hejase, H.A., Noura, H.M., Fardoun, A.A. (Eds.), ICREGA'14 - Renewable Energy: Generation and Applications. Springer International Publishing, Cham, pp. 299–313.

Kaiser, M.S., Iida, T., Taniguchi, T., Katayama, T., Yoshimura, R., Irifune, K., 2025. Optimal prediction horizon length in model predictive control to maximise energy absorption by a point absorber wave energy converter. Ocean Eng. 329, 121130. http://dx.doi.org/10.1016/j.oceaneng.2025.121130, URL https://www.sciencedirect.com/science/article/pii/S0029801825008431.

Kashiwagi, M., Ten, I., Yasunaga, M., 2006. Hydrodynamics of a body floating in a two-layer fluid of finite depth. part 2. Diffraction problem and wave-induced motions. J. Mar. Sci. Technol. 11, 150–164. http://dx.doi.org/10.1007/s00773-005-0212-3.

Kelly, J., O'Sullivan, D., Wright, W., Alcorn, R., Lewis, A., 2014. Challenges and lessons learned in the deployment of an offshore oscillating water column. COMPEL - Int. J. Comput. Math. Electr. Electron. Eng. 33 (5), 1678–1704. http://dx.doi.org/10.1108/COMPEL-09-2013-0307.

Khedkar, K., Bhalla, A.P.S., 2022. A model predictive control (MPC)-integrated multiphase immersed boundary (IB) framework for simulating wave energy converters (WECs). Ocean Eng. 260, 111908. http://dx.doi.org/10.1016/j.oceaneng.2022.111908, URL https://www.sciencedirect.com/science/article/pii/S0029801822012471.

Korde, U., Ertekin, R., 2015. Wave energy conversion by controlled floating and submerged cylindrical buoys. J. Ocean. Eng. Mar. Energy 1, 255–272. http://dx.doi.org/10.1007/s40722-015-0021-7.

Li, G., Belmont, M.R., 2014. Model predictive control of sea wave energy converters – part I: A convex approach for the case of a single device. Renew. Energy 69, 453–463. http://dx.doi.org/10.1016/j.renene.2014.03.070.

Li, S., Li, K., Rajamani, R., Wang, J., 2011. Model predictive multi-objective vehicular adaptive cruise control. IEEE Trans. Control Syst. Technol. 19 (3), 556–566. http://dx.doi.org/10.1109/TCST.2010.2049203.

Li, D., Patton, R.J., 2023. Model following robust control of a wavestar-prototype wave energy converter: Part 2 estimation and optimal reference computation. IFAC-PapersOnLine 56 (2), 11729–11734. http://dx.doi.org/10.1016/j.ifacol.2023.10.541, URL https://www.sciencedirect.com/science/article/pii/S2405896323009084, 22nd IFAC World Congress.

Liang, H., Qin, H., Su, H., Wen, Z., Mu, L., 2024. Environmental-sensing and adaptive optimization of wave energy converter based on deep reinforcement learning and computational fluid dynamics. Energy 297, 131254. http://dx.doi.org/10.1016/j.energy.2024.131254, URL https://www.sciencedirect.com/science/article/pii/S0360544224010272.

Ling, B.A., Bosma, B., Brekken, T.K.A., 2020. Experimental validation of model predictive control applied to the azura wave energy converter. IEEE Trans. Sustain. Energy 11 (4), 2284–2293. http://dx.doi.org/10.1109/TSTE.2019.2953868.

Montoya Andrade, D.-E., de la Villa Jaén, A., García Santana, A., 2014. Considering linear generator copper losses on model predictive control for a point absorber wave energy converter. Energy Convers. Manage. 78, 173–183. http://dx.doi.org/10.1016/j.enconman.2013.10.037, URL https://www.sciencedirect.com/science/article/pii/S0196890413006729.

MSCI, 2023. Global primary energy consumption in 2023. https://www.msci-institute.com/charts/global-primary-energy-consumption-generation-in-2023/, (Accessed 13 September 2025).

Murai, M., Iikura, H., 2020. Consideration on how to decide the optimal control force of a PA-WEC for maximizing its electric power generation in irregular waves. J. Jpn. Soc. Nav. Archit. Ocean. Eng. 31, 73–81. http://dx.doi.org/10.2534/jjasnaoe.31.73.

Muraleedharan, G., Lucas, C., Soares, C.G., 2023. Spectral wave energy period and peak period statistics concomitant with maximum significant wave heights. Coast. Eng. 183, 104260. http://dx.doi.org/10.1016/j.coastaleng.2022.104260, URL https://www.sciencedirect.com/science/article/pii/S0378383922001739.

Naito, S., Nakamura, S., 1986. Wave energy absorption in irregular waves by feedforward control system. In: Evans, D.V., de Falcão, A.F.O. (Eds.), Hydrodynamics of Ocean Wave-Energy Utilization. Springer Berlin Heidelberg, Berlin, Heidelberg, pp. 269–280.

Newman, J.N., 1977. Marine Hydrodynamics. The MIT Press, http://dx.doi.org/10.7551/mitpress/4443.001.0001.

Nguyen, H.-N., Sabiron, G., Tona, P., Kramer, M.M., Vidal Sanchez, E., 2016. Experimental validation of a nonlinear MPC strategy for a wave energy converter prototype. In: International Conference on Offshore Mechanics and Arctic Engineering, Volume 6: Ocean Space Utilization; Ocean Renewable Energy, http://dx.doi.org/10.1115/OMAE2016-54455, V006T09A019.

Nguyen, H.-N., Tona, P., 2018. Wave excitation force estimation for wave energy converters of the point-absorber type. IEEE Trans. Control Syst. Technol. 26 (6), 2173–2181. http://dx.doi.org/10.1109/TCST.2017.2747508.

Osinenko, P., Dobriborsci, D., 2021. Effects of sampling and prediction horizon in reinforcement learning. IEEE Access 9, 127611–127618. http://dx.doi.org/10.1109/ACCESS.2021.3112498.

O'Sullivan, A.C., Lightbody, G., 2017. Co-design of a wave energy converter using constrained predictive control. Renew. Energy 102, 142–156. http://dx.doi.org/10.1016/j.renene.2016.10.034, URL https://www.sciencedirect.com/science/article/pii/S0960148116308990.

Pizer, D., 1993. Maximum wave-power absorption of point absorbers under motion constraints. Appl. Ocean Res. 15 (4), 227–234. http://dx.doi.org/10.1016/0141-1187(93)90011-L.

Reabroy, R., Zheng, X., Zhang, L., Zang, J., Yuan, Z., Liu, M., Sun, K., Tiaple, Y., 2019. Hydrodynamic response and power efficiency analysis of heaving wave energy converter integrated with breakwater. Energy Convers. Manage. 195, 1174–1186. http://dx.doi.org/10.1016/j.enconman.2019.05.088, URL https://www.sciencedirect.com/science/article/pii/S0196890419306430.

Ringwood, J.V., Bacelli, G., Fusco, F., 2014. Energy-maximizing control of wave-energy converters: The development of control system technology to optimize their operation. IEEE Control Syst. Mag. 34 (5), 30–55. http://dx.doi.org/10.1109/MCS.2014.2333253.

Sergiienko, N.Y., Cocho, M., Cazzolato, B.S., Pichard, A., 2021. Effect of a model predictive control on the design of a power take-off system for wave energy converters. Appl. Ocean Res. 115, 102836. http://dx.doi.org/10.1016/j.apor.2021.102836.

Sierra, J., Mösso, C., González-Marco, D., 2014. Wave energy resource assessment in menorca (Spain). Renew. Energy 71, 51–60. http://dx.doi.org/10.1016/j.renene.2014.05.017, URL https://www.sciencedirect.com/science/article/pii/S0960148114002687.

Tan, J., Polinder, H., Laguna, A.J., Miedema, S., 2022. A numerical study on the performance of the point absorber wave energy converter integrated with an adjustable draft system. Ocean Eng. 254, 111347. http://dx.doi.org/10.1016/j.oceaneng.2022.111347, URL https://www.sciencedirect.com/science/article/pii/S0029801822007375.

Tobar Fuentes, K., Ledezma, C., 2024. Effects of dynamic load application, irregular wave conditions, and base flexibility on the structural response of a vertical pile platform. Ocean Eng. 304, 117919. http://dx.doi.org/10.1016/j.oceaneng.2024.117919, URL https://www.sciencedirect.com/science/article/pii/S0029801824012575.

Todalshaug, J., Falnes, J., Moan, T., 2011. Constrained optimal control of a heaving buoy wave-energy converter. J. Offshore Mech. Arct. Eng. 133, 011401. http://dx.doi.org/10.1115/1.4001431.

Umeda, J., Taniguchi, T., Katayama, T., 2024. Experimental validation of data-driven reactive control strategy for wave energy converters: A Gaussian process regression approach. Ocean Eng. 308, 118264. http://dx.doi.org/10.1016/j.oceaneng.2024.118264.

Wu, Q., Tan, J., Jin, X., Zhang, M., Turk, A., 2022. Chapter 11 - MPC-based real-time operation of integrated energy systems. In: Wu, Q., Tan, J., Jin, X., Zhang, M., Turk, A. (Eds.), Optimal Operation of Integrated Multi-Energy Systems under Uncertainty. Elsevier, pp. 295–337. http://dx.doi.org/10.1016/B978-0-12-824114-1.00002-0, URL https://www.sciencedirect.com/science/article/pii/B9780128241141000020.

Yang, Q., Karamanakos, P., Geyer, T., Kennel, R., 2021. A direct model predictive control strategy with optimized sampling interval. In: 2021 IEEE International Conference on Predictive Control of Electrical Drives and Power Electronics. PRECEDE, pp. 268–274. http://dx.doi.org/10.1109/PRECEDE51386.2021.9680882.

Yin, X., Jiang, Z., 2023. Wave condition preview assisted real-time nonlinear predictive control of point-absorbing wave energy converter based on long short-term memory recurrent neural identification. Mech. Syst. Signal Process. 188, 109669. http://dx.doi.org/10.1016/j.ymssp.2022.109669, URL https://www.sciencedirect.com/science/article/pii/S0888327022007506.

Yoshimura, R., Iida, T., Kaiser, M.S., Irifune, K., 2025. Fast real-time prediction of wave exciting force for a point absorber based on impulse response functions. Appl. Ocean Res. 158, 104539. http://dx.doi.org/10.1016/j.apor.2025.104539, URL https://www.sciencedirect.com/science/article/pii/S0141118725001270.

Zhang, M., Yu, S.-R., Zhao, G.-W., Dai, S.-S., He, F., Yuan, Z.-M., 2024. Model predictive control of wave energy converters. Ocean Eng. 301, 117430. http://dx.doi.org/10.1016/j.oceaneng.2024.117430, URL https://www.sciencedirect.com/science/article/pii/S0029801824007674.

Zhang, Y., Zhao, Y., Sun, W., Li, J., 2021. Ocean wave energy converters: Technical principle, device realization, and performance evaluation. Renew. Sustain. Energy Rev. 141, 110764. http://dx.doi.org/10.1016/j.rser.2021.110764.

Zou, S., Zhou, X., Khan, I., Weaver, W.W., Rahman, S., 2022. Optimization of the electricity generation of a wave energy converter using deep reinforcement learning. Ocean Eng. 244, 110363. http://dx.doi.org/10.1016/j.oceaneng.2021.110363, URL https://www.sciencedirect.com/science/article/pii/S0029801821016590.

Zullah, M.A., Lee, Y.-H., 2013. Performance evaluation of a direct drive wave energy converter using CFD. Renew. Energy 49, 237–241. http://dx.doi.org/10.1016/j.renene.2012.01.023, URL https://www.sciencedirect.com/science/article/pii/S0960148112000341, Selected papers from World Renewable Energy Congress - XI.